

Mid-Infrared Wavelength Tunable Resonant Cavity Enhanced Detectors

A dissertation submitted to

ETH ZURICH

for the degree of
Doctor of Sciences

presented by

FERDINAND FELDER

Dipl.-Ing. TU Wien
born June 8th 1978
citizen of Germany

accepted on the recommendation of:

PD. Dr. Hans Zogg, examiner

Prof. Dr. Danilo Pescia, co-examiner

Prof. Dr. Jürg Dual, co-examiner

Contents

Abstract	iii
Zusammenfassung	v
1 Introduction	1
1.1 Motivation	1
1.2 Thin Film Materials and Deposition	4
1.3 Heterostructures	7
1.4 Characterization Methods	9
2 Tunable RCED	13
2.1 Working Principle	13
2.2 Optical Characteristics	15
2.3 Diode Chip	23
2.3.1 Layer Stack Design	23
2.3.2 High Sensitivity of Thin Photodiodes	27
2.4 MEMS Micro-mirror	30

2.5	Practical Limitations	34
2.6	Tunable RCED Devices	40
2.6.1	PbTe RCED	41
2.6.2	PbSrTe RCED for Shorter Wavelengths	48
2.6.3	PbSnTe RCED for Longer Wavelengths	50
3	PbTe Quantum Dots	53
3.1	Transition Energies	54
3.2	Formation of PbTe QD	56
4	Conclusion	63
	Appendix – MIR Absorption lines	65
	Bibliography	76
	Publications	77
	Acknowledgements	87

Abstract

This thesis deals with the realization of a novel type of tunable detector. It is sensitive in the mid-infrared wavelength region, which is technologically interesting for applications including gas spectroscopy and thermal imaging. The presented detectors have favorable properties: a narrow spectral peak bandwidth, a high quantum efficiency, and a low noise. In addition, the detection peak can be actively tuned over a broad wavelength region. The size of a detector is very small, essentially allowing the fabrication of a *spectrometer on a chip*.

This miniaturization is made possible by applying the principle of a resonant cavity enhanced detector (RCED). Here, the photosensitive absorber is placed within a cavity formed by two mirrors. Incoming radiation is reflected multiple times within the cavity, and a standing wave pattern is formed. The detection signal originates almost exclusively from these resonances. With the appropriate material composition all but one resonance peak can be suppressed, yielding a single-mode detector. The resonance condition changes in relation to the cavity length. By altering the cavity length, the wavelength of the detection peak can be actively tuned.

The device consists of two chips, fabricated separately: one with the first mirror and the photodiode, the other with the movable top mirror. Both are manufactured on wafer level, yielding a high chip output, and then integrated in a final process step. The diode chip with the photosensitive pn^+ heterojunction and the first mirror is grown epitaxially on a sil-

icon substrate. The narrow gap IV–VI semiconductor PbTe and ternary alloys thereof are used. Lead–salts have favorable properties for opto–electronic devices in the mid–infrared, such as a low Auger recombination rate and a very high refractive index. Their bandgap is chemically tunable over a very wide range. The second chip is a movable micro–mirror realized using a micro–electro–mechanical system (MEMS). It is fabricated by the Center of Mechanics at ETH Zurich. Its silicon membrane can be vertically moved by electrostatic forces. Depending on actuation voltage the cavity length is changed, thus shifting the detection wavelength.

Different RCED device setups were realized, illustrating the advantages of the RCED concept and of the material system. Devices using a PbTe absorber layer were designed for a narrow peak width and high operation temperatures. They are sensitive at $\sim 5 \mu\text{m}$ wavelength when operating at 120 K and at $\sim 4 \mu\text{m}$ for 240 K. The wavelength tuning range is $0.5 \mu\text{m}$ wide for single–mode detection. The linewidth of the detection peak is 35 nm, limited by the measurement setup. Other devices achieved shorter and longer wavelengths by chemical tuning. A RCED with a PbSrTe absorber is sensitive down to $\sim 3.4 \mu\text{m}$, while another with a PbSnTe absorber is sensitive up to $\sim 7.7 \mu\text{m}$.

As a possible further improvement, a quantum dot infrared photodetector may be incorporated within a RCED. For a traditional detector setup, the density of the quantum dots has to be extremely high to yield a good absorption. In a RCED, however, the density may be lower since, here, photons entering the cavity are reflected multiple times between the mirrors until they are absorbed by the detector layer. As a preliminary step, the formation of PbTe quantum dots in a CdTe host on silicon (111) substrate was studied as well.

Zusammenfassung

Die vorliegende Arbeit beschreibt die Herstellung eines neuartigen durchstimmbaren Infrarot-Detektors. Anwendungen wie Gasspektroskopie und Wärmebilder machen diesen Wellenlängenbereich technologisch interessant. Die vorgestellten Detektoren haben hervorragende Eigenschaften: Sie sind schmalbandig empfindlich, haben eine hohe Quantenausbeute und ein geringes Rauschen. Zusätzlich sind sie über einen breiten Wellenlängenbereich durchstimmbare. Aufgrund der geringen Abmessungen des Bauteils kann man von einem *Spektrometer auf einem Chip* sprechen.

Möglich wird diese Miniaturisierung durch das Prinzip eines resonanzverstärkten Detektors (resonant cavity enhanced detector, RCED). Hierbei handelt es sich um einen photoaktiven Absorber der innerhalb einer Kavität, begrenzt von zwei Spiegeln, platziert ist. Einfallende Strahlung wird mehrfach innerhalb der Kavität gespiegelt und eine stehende Welle bildet sich aus. Durch unterschiedliche Materialzusammensetzungen können alle Resonanzen bis auf eine unterdrückt werden. Das detektierte Signal stammt dann fast ausschliesslich von dieser verbleibenden Resonanz. Da die Resonanzbedingung von der Kavitätslänge abhängt kann durch Ändern dieser die Wellenlänge des detektierten Resonanzmaximums aktiv durchgestimmt werden.

Ein RCED besteht aus zwei getrennt gefertigten Chips, der eine mit dem ersten Spiegel und der Photodiode, der andere mit dem zweiten, beweglichen Spiegel. Bei der Herstellung er-

hält man pro Wafer eine grosse Anzahl an Chips, welche erst in dem letzten Prozessschritt gebondet werden. Der Diodenchip besteht aus dem photoaktiven pn^+ Heteroübergang und einem der zwei Spiegel. Hierfür werden Bleitellurid, ein IV–VI Halbleiter mit schmaler Bandlücke, und ternäre Verbindungen davon epitaktisch auf Siliziumsubstrat gewachsen. Diese Bleisalze haben eine geringe Auger–Rekombinationsrate und einen hohen Brechungsindex. Sie sind daher gut für den Einsatz in optoelektronischen Infrarot–Bauteilen geeignet. Die Bandlücke von Bleisalzen lässt sich ausserdem chemisch über einen sehr weiten Wellenlängenbereich verschieben. Der zweite Chip ist ein beweglicher Mikrospiegel, ein mikro–elektro–mechanisches System (MEMS) realisiert von dem Zentrum für Mechanik der ETH Zürich. Seine Siliziummembran kann durch elektrostatische Kräfte vertikal bewegt werden. Abhängig von der Anregungsspannung ändert sich so die Kavitätslänge und die Wellenlänge des detektierten Resonanzmaximums wird verschoben.

Zur Veranschaulichung der Vorteile des RCED Prinzips und des Materialsystems wurden verschiedene RCED verwirklicht. Bauteile mit einem PbTe Absorber weisen eine schmale Breite des Resonanzmaximums auf und sind für hohe Betriebstemperaturen entworfen. Bei einer Betriebstemperatur von 120 K sind sie bei einer Wellenlänge von $\sim 5 \mu\text{m}$ empfindlich, bei 240 K hingegen bei $\sim 4 \mu\text{m}$. Der durchstimmbare Bereich ist $0.5 \mu\text{m}$ breit, bei einer einzelnen detektierten Resonanz mit einer Linienbreite von 35 nm. Weitere Bauteile sind aufgrund chemischer Zusammensetzung des PbSrTe Absorbers bei kürzeren Wellenlängen bis $\sim 3.4 \mu\text{m}$ empfindlich. Mit einem PbSnTe Absorber wurden längere Wellenlängen bis $\sim 7.7 \mu\text{m}$ erreicht.

Eine mögliche Weiterentwicklung ist die Verwendung eines Quantenpunkt–Detektors innerhalb der Kavität. In einem herkömmlichen Detektor muss die Dichte der Quantenpunkte für eine gute Absorption sehr hoch sein. In einem RCED hingegen ist bereits eine wesentlich geringere Dichte ausreichend, da hier die einfallende Strahlung mehrfach den Absorber passiert und deshalb quasi vollständig absorbiert wird. Als Voruntersuchung wurde die Entstehung von PbTe Quantenpunkten in einer CdTe Matrix auf Silizium Substrat untersucht.

Chapter 1

Introduction

1.1 Motivation

The mid-infrared wavelength region (MIR, 3–10 μm) offers various possibilities for applications and is therefore technologically interesting. While water has a transparency window in the MIR, combustion gases and hydrocarbons exhibit very strong absorption lines. Gas spectroscopy sensors therefore offer a very high sensitivity when operating in the MIR. Possible applications include environmental monitoring, combustion exhaust and efficiency, and industrial process control [1, 2]. The absorption lines of the relevant gases are listed in the appendix. Furthermore, thermal imaging sensors allow night vision and surveillance products, as well as building inspection concerning thermal leaks [3, 4].

State-of-the-art MIR detectors exhibit a large signal-to-noise ratio [3]. They are operating at temperatures achievable by Peltier effect electric cooling or above. Commercially available multi-stage Peltier elements yield a temperature difference of ~ 100 K [5]. Adaptive focal plane arrays are additionally selectively sensitive at a constrained spectral range. Furthermore, the size of the detector should be reasonable small to allow the integration within a portable system. As presented in the fol-

lowing, a MIR detector offering all these required features can be realized in a very elegant way using the principle of a resonant cavity enhanced detector (RCED) [6].

A RCED is basically an optical Fabry–Pérot cavity formed by two mirrors with an absorber placed inside. Incoming radiation is reflected multiple times within the cavity and a standing wave pattern is formed. The detection signal originates almost exclusively from these resonances. By adapting the cavity length the detected resonance wavelength can be directly tuned. This change of cavity length can be achieved in a very compact way by employing a vertically movable micro–electro–mechanical system (MEMS) micro–mirror [7]. With the appropriate material composition all but one detection peak can be suppressed. The final device then has a single detection peak, which can be shifted deliberately over a broad wavelength region. A tunable RCED therefore is essentially a spectrometer on a chip.

The narrow bandgap IV–VI semiconductors employed in this work, PbTe and alloys thereof, are very favorable for opto–electronic devices in the MIR [8]. By combining structural simplicity and flexibility they offer a decent alternative to other material systems. Monolithic RCED using IV–VI materials have already been realized [9,10,11]. Schottky–diodes were used with either PbEuSe or PbSnSe as absorber layer. They exhibit a single detection peak at 4.1 μm , or two peaks at 7.3 μm and 8.4 μm respectively. Peak quantum efficiency is above 50%, even without an anti–reflection coating on the silicon substrate. Despite the fixed cavity length they are tunable by temperature to some extent. The feasibility of a RCED tunable via an external cavity was shown as well [11]. Here a p–PbTe/n⁺–PbSrTe heterojunction and a piezo actuated top mirror were used. The basic procedures published there are also used in this work. Furthermore, two–dimensional focal plane arrays with a PbTe absorber grown epitaxially on silicon read–out chips have been realized [12].

Monolithic RCED using the II–VI semiconductor Hg_{1-x}Cd_xTe (MCT) or III–V materials are sensitive only for MIR radiation shorter than 3 μm [13,14,15]. Also their characteristics are lack-

ing in terms of peak width and signal-to-noise contrast. However, in a more complex setup employing three cavities, a very narrow line width has been achieved [16]. A working example of a tunable RCED with an external cavity has been described for infrared radiation shorter than 1 μm [17].

In a competitive approach to build a tunable detector a separated filter in front of a broadband detector has been used [18, 19, 20, 21]. This filter can be a wavelength-selective grating or an optical cavity. Any detector with a broad spectral response is suited for this tandem approach. However, due to the use of a conventional photodetector instead of an integrated internal absorber layer, the theoretical limit of the signal-to-noise ratio of such a setup is inferior when compared to a RCED.

Many currently commercially available broadband MIR detectors are based on II-VI MCT absorber layers. The dependence of bandgap on MCT material composition is however inconveniently steep, making a precise control of the cut-off wavelength difficult [22]. MIR detectors have also been built using more complex sample structures with III-V semiconductors. Infrared focal plane arrays (IRFPA) using III-V quantum dot infrared photodetectors (QDIP) have been described [23, 24]. Furthermore, quantum cascade detectors (QCD) operating at room temperature with a very fast reaction time have been realized [25]. Their complex structure consists of up to several hundred layers. Their sensitivity curve is generally narrow and its wavelength is fixed during growth. Tuning is therefore only very limited possible via operation temperature. When compared to intrinsic detector materials, the quantum efficiency of QCD intersubband transitions is much lower. Recently a tandem QCD with a broad spectral response has been demonstrated [26].

As a possible further advancement of the RCED concept, a QDIP or a quantum well detector may be incorporated within the resonant cavity. QDIP have high sensitivity limits due to the long lifetimes of photo-excited carriers [27]. A major disadvantage of QDIP is their low quantum efficiency due to a very low absorption, mainly caused by a low quantum dot (QD) density. This can be overcome by employing the QDIP within a resonant cavity [28]. Monolithic RCED with a photosensi-

tive IV–VI PbTe/PbEuTe quantum well structure have already been realized [29]. Quantum well infrared detectors are sensitive only to radiation of certain polarizations. Therefore special light coupling is needed, decreasing efficiency and increasing cost.

Epitaxial IV–VI QD with a pyramidal shape in (111) oriented layers, e.g. PbSe QD in a PbTe(111) host, have already been studied [30, 31, 32]. Diffusion leads to a truncation of the pyramidal QD. This effect was greatly reduced when alloying the host with Sr or covering the QD with a very thin EuTe film before continuing with the IV–VI overgrowth. Photoconductivity in such layers has been demonstrated, too [33]. In a different approach coherent PbTe or PbSnTe QD in a CdTe(100) host on lattice mismatched GaAs(100) were obtained [34, 35, 36]. The size of the QD were adjusted by annealing conditions, while their shape was highly symmetric cubo–octahedral. PbTe and SnTe QD were also achieved by ion implantation, again in a CdTe(100) matrix [37]. The here presented work discusses the formation of self–assembled PbTe QD in a CdTe(111) matrix on silicon substrate.

1.2 Thin Film Materials and Deposition

The lead–chalcogenide PbTe and related compounds are used. Lead–salts are narrow gap IV–VI semiconductors with an absorption edge ranging from 3 μm to 40 μm , depending on composition and temperature [8]. Additionally they have a very low Auger recombination rate, which is especially important for low thermal noise [38, 39]. IV–VI semiconductors are therefore very favorable for opto–electronic devices and applications in the MIR. EuTe is used as complementary material with a low refractive index for Bragg reflectors. Fundamental properties of the used materials are listed in table 1.1.

The bandgap of IV–VI materials depends heavily on material composition and temperature. As shown in figure 1.1 the bandgap can be engineered to shorter or longer wavelengths by

	Lattice constant [Å]	Cut-off wavelength at 100 K [μm]	Refractive index n at 100 K, 5 μm	Linear thermal expansion at 300 K [10 ⁻⁶ K ⁻¹]	References
PbTe	6.46	5.6	6.3	19.8	[40, 41, 42]
Pb _{0.99} Eu _{0.01} Te	>	4.5	5.9	–	[43, 44]
Pb _{0.99} Sr _{0.01} Te	>	4.7	6.1	–	[45]
Pb _{0.99} Sn _{0.01} Te	<	5.7	6.3	–	[46, 47]
EuTe	6.59	~0.6	2.4	13.6	[48, 49]
CdTe	6.48	~0.8	2.7	5.3	[50, 51, 52]
Si	5.43	~1.11	3.42	2.6	[53, 54, 55]
BaF ₂	6.19	~0.11	1.45	19.8	[56, 57, 58]
CaF ₂	5.46	~0.15	1.4	18.9	[56, 57, 58]

Table 1.1: Properties of the used materials.

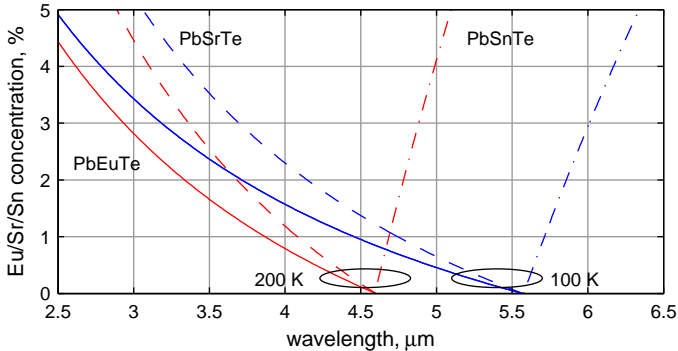


Figure 1.1: Dependency of the cut-off wavelength of $Pb_{1-x}Eu_xTe$, $Pb_{1-x}Sr_xTe$, and $Pb_{1-x}Sn_xTe$ on material composition. With increasing temperature it is shifted towards shorter wavelengths.

forming ternary alloys of PbTe. Alloying with Eu and Sr decreases the bandgap wavelength, while adding Sn increases it. When compared to $\text{Hg}_{1-x}\text{Cd}_x\text{Te}$ the dependence of bandgap on composition is much less pronounced, allowing a much more precise control of the cut-off wavelength. The bandgap also changes with temperature, but contrary to most other semiconductors its wavelength increases with decreasing temperature. A temperature change from room temperature down to 100 K shifts the cut-off wavelength of PbTe from slightly below 4 μm up to 5.6 μm .

The refractive index of lead-salts is composition and temperature dependent as well. For alloying with Eu and Sr it is decreasing with higher concentrations, while it increases when more Sn is added. This effect can be used to engineer an antireflection layer with the ideal refractive index. With increasing temperature the refractive index generally decreases.

The wide-gap II-VI semiconductor CdTe is used as a host matrix for PbTe QD. PbTe is nearly lattice matched to CdTe. Both have a face-centered cubic (fcc) translation symmetry, but while PbTe has a rock salt crystal structure, CdTe crystallizes in the zinc blende structure. Due to the different crystal structure PbTe precipitates can form without intermixing by phase separation [59, 35]. The valence band offset of PbTe and CdTe is 0.135 eV [60].

The samples are grown by molecular beam epitaxy (MBE) on silicon(111) substrate. Solid source thermal effusion cells are used for evaporation of the compound or single element materials. Thickness and composition of the layers are controlled by flux ratios. PbTe p-type conductivity is ensured by an excess Te flux and n⁺ doping is achieved by adding Bi. The interfaces between differently doped regions are sharp [61]. Within the MBE chamber in situ reflection high-energy electron diffraction (RHEED) observations are possible. RHEED images with streaks indicate 2D layer-by-layer growth, while points indicate a 3D island growth mode.

The thermal expansion coefficients as well as the lattice constants of silicon and lead-salts are quite different. This yields

an induced stress when cooling down from growth temperature to room temperature or below. For (111) orientated lead–salts this stress relaxes along the (100)–type glide planes [62]. The planes are inclined with an angle of 54° in respect to the surface. The strain therefore has a lateral component along those glide planes, allowing the relaxation of the layer. The growth in (111) orientation is ensured by a very thin layer of CaF_2 deposited on the silicon. An additional BaF_2 buffer layer is used to grow CdTe on silicon [63]. It is completely strain relieved in films thicker than 250 nm [64].

Additional layers needed for the final device are deposited at a later stage during processing. This is done in different chambers under UHV or HV conditions using electric current or an electron beam for thermal evaporation of the source material. The deposited layers are polycrystalline or amorphous. Materials used are Te as transparent electric contact (refractive index $n = 4.37$) and ZnSe as antireflection coating ($n = 2.4$). Gold is used as electric contact and as reflective coating of the MEMS micro–mirror. Its reflectivity in the MIR wavelength region is greater than 99.3% [65,66]. Even though the reflectivity of aluminum is even higher, gold was chosen due to process reasons.

1.3 Heterostructures

Distributed Bragg Reflector

Distributed Bragg reflectors (DBR) are an important component of optical devices [67]. They consist of multiple pairs of alternating high and low refractive index layers. Incoming rays are reflected at each interface. They interfere with each other, depending on path length and phase shift (π for an interface of low to high refractive index). For an optical thickness of each individual layer of $\lambda/4$ the reflected beams interfere constructively. The maximum reflectivity increases with the number of layers and with the refractive index contrast of the materials used. Furthermore, with a high index contrast the stopband widens and high reflectivity is observed over a broader band of

the spectrum.

Lead-salts have an extremely high refractive index and are therefore very well suited for DBR. In conjunction with EuTe the index contrast is $n_1/n_2 = 2.6$. This is much higher than the typical value of $n_1/n_2 \approx 1.1$ for the materials employed in II-VI and III-V DBR. While there typically 20 or more pairs of layers are required for an useful high reflectivity, with lead-salts already a small number of layers is sufficient [68]. Figure 1.2 compares the calculated reflectivity of $\text{Pb}_{0.99}\text{Sr}_{0.01}\text{Te}/\text{EuTe}$ stacks for different numbers of layers. The design wavelength is $5 \mu\text{m}$ with an operation temperature of 120K. The calculated maximum reflectivity is greater 95%, 99.2% and 99.9% for 1.5, 2.5 and 3.5 layer pairs, respectively. The edge in the reflection curves at $4.6 \mu\text{m}$ correlates to the cut-off wavelength of $\text{Pb}_{0.99}\text{Sr}_{0.01}\text{Te}$ at 120 K.

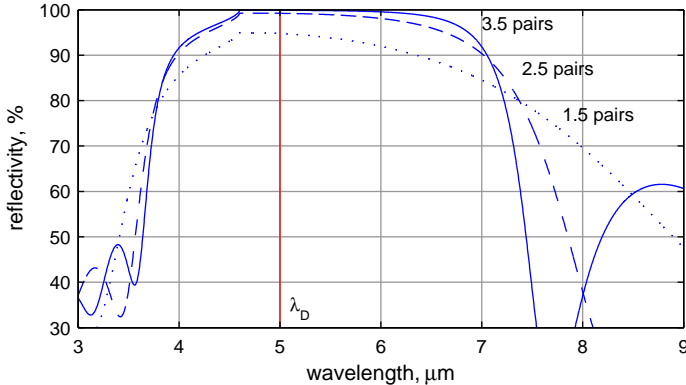


Figure 1.2: Calculated reflectivity of $\text{Pb}_{0.99}\text{Sr}_{0.01}\text{Te}/\text{EuTe}$ DBR with 1.5, 2.5 and 3.5 layer pairs on Si as a function of wavelength. The corresponding maximum values at the design wavelength of $5 \mu\text{m}$ and 120 K operation temperature are greater 95%, 99.2% and 99.9%.

Antireflection Coating

Similar to a DBR an anti reflection (AR) coating can be achieved as well using interference effects [67]. In case of the RCED a single layer PbEuTe with an optical thickness of $\lambda/4$ is used as AR to reduce unwanted resonance effects of the external buffer layer. Its refractive index is engineered by material composition to be $n_{AR} = \sqrt{n_{Si} \cdot n_{PbSrTe}}$ for the particular target wavelength and operating temperature. Most often the refractive index is not adjustable. In this case a multilayer AR coating can be designed for the given materials.

1.4 Characterization Methods

Electronic Properties

The Hall mobility and carrier concentration of the grown layer stack are important indicators for the electrical quality of the final device. The measurement method described by van–der–Pauw is used, with a square sample geometry [69, 70]. The samples are cooled down to 10 K in a closed cycle He cryostat.

The sensitivity of a photovoltaic infrared sensor is determined by the noise current densities. It can be quantified by the R_0A product, which is the differential resistance at zero bias R_0 , derived from a current–voltage (IV) curve measured without illumination, multiplied with the area of the diode A . From the R_0A other important characteristics like the detectivity and D^* can be derived [71].

Crystal quality, Structure and Composition

The electric properties of lead salts at low temperatures are dominated by defect carrier scattering. As a consequence the Hall mobility increases for decreasing temperatures until it saturates at its maximum. Hence the low temperature Hall mobility

allows to determine the dislocation density and to conclude on the crystal quality [72].

The crystal structure and surface composition is analyzed using Scanning Electron Microscopy (SEM). The brightness of an image taken with back scattered electrons depends on the material composition at the surface and slightly below it. With a tilted view angle the contribution of surface roughness on image contrast can be reduced. Higher resolutions are achieved with Scanning Transmission Electron Microscopy (STEM). Both techniques allow the determination of elements using energy dispersive X-ray spectroscopy (EDX). All SEM and STEM investigations were performed by EMEZ – Electron Microscopy ETH Zurich [73].

Further information on the surface morphology is gathered using an atomic force microscope. Due to the PbTe(111) growth the samples show a threefold symmetry.

Optical Properties

The optical characteristics of the layer stack are calculated before growth [11]. Of main interest are DBR reflectivity, spectral response of a RCED and the field intensity within the cavity. The transfer-matrix method as described by Macleod is used [67]. It works by computing the forward and backward traveling waves at each interface. Input parameters are the intended operation temperature and the thickness of each layer. The temperature and composition dependent refractive index and absorption coefficient are taken from literature, see table 1.1.

Reflectivity and transmission spectra of each grown layer stack are measured with a Fourier-transform infrared spectrometer (FTIR). Its spectral resolution is 1 cm^{-1} , which translates to 2.5 nm at a wavelength of 5 μm . The calculated transmission and reflection spectra correspond very well to the experimental data [own publications, article 1]. The FTIR is also used to measure the wavelength-dependent quantum efficiency signal of the detector devices. The calibration measurements were per-

formed with a 500 K blackbody radiator and using a monolithic RCED as reference device [9]. With an additional external InSb IR–detector photoluminescence (PL) spectra of QD samples are recorded. A commercial laser emitting at 1.55 μm is used for optical pumping.

Chapter 2

Tunable RCED

2.1 Working Principle

The working principle of a tunable RCED is shown in figure 2.1. A RCED consists of two mirrors with corresponding reflectivities R_i forming a Fabry–Pérot cavity. An absorber layer with a thickness d and an absorption coefficient α is embedded within the cavity. All other α_i are generally negligible small. Incoming radiation is reflected back and forth within the cavity. The optical cavity length is the sum of all thicknesses multiplied with the corresponding refractive index $L_{opt} = \sum n_i d_i$. A phase shift ψ_i occurs on reflection, depending on the mirror type. As discussed in the following section 2.2, the effective cavity length differs from the optical length due to these phase shifts. Tunability is achieved by changing the cavity length with a movable top mirror.

Within the cavity a standing wave pattern forms depending on effective cavity length. For resonance wavelengths the optical field is enhanced, otherwise it is lowered. The detected signal then originates almost exclusively from the narrow resonances. This optical field enhancement effect yields a significantly improved signal-to-noise ratio for wavelengths with constructive interference. Due to the multiple passes of the radiation within

the cavity a high absorption and quantum efficiency is achieved, even for a very thin absorber layer. Such a thin absorber has a much smaller volume in which noise can be generated, further improving the signal-to-noise ratio. This is a major advantage of a RCED in comparison with a conventional broadband photo detector coupled with a tunable band-pass filter. It is discussed in detail in section 2.3.2.

The lower mirror is a DBR. It is not absorbing to allow radiation to enter the cavity. On top of the mirror is the absorbing photodiode. This diode chip is described in section 2.3.1. The movable top mirror is realized using a MEMS micro-mirror with a highly reflective gold coating, see section 2.4. It is fabricated by the Center of Mechanics at ETH Zurich [74]. Chip output of both, the diode chip and the MEMS chip, is high due to fabrication at wafer level. The chips are bonded together in a final processing step, using the photoresist SU-8 as adhesive spacer layer. Its thickness, typically 10–20 μm , can be chosen during processing, thus defining the initial length of the external cavity.

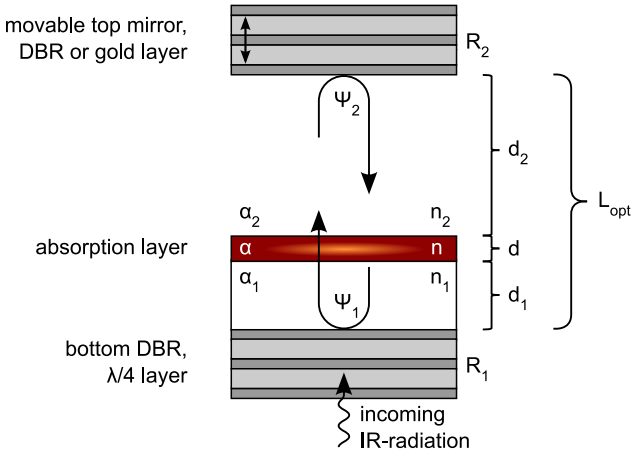


Figure 2.1: Working principle of a tunable RCED. Due to resonance effects the absorber layer within the Fabry-Pérot cavity can be very thin, while high quantum efficiency is maintained.

2.2 Optical Characteristics

The optical characteristics of a RCED are partly in competition to each other and not all can be optimized at the same time. Of great importance is the maximum achievable quantum efficiency. The free spectral range (FSR) is the distance between two resonance peaks. It limits the maximum wavelength range over which single mode tuning is possible. The width at half maximum (FWHM) of a peak limits the resolution of spectroscopic applications. The optical characteristics of the RCED are determined by the properties of its cavity. Most influential are the effective length of the cavity, the finesse, and the absorbance within the cavity. The finesse depends mainly on the mirror reflectivities, but also on deviations of mirror plane parallelism and on surface roughness. Ideally only the photodiode is absorbing within the cavity.

The following calculations are performed with the realized RCED devices in mind using the example of a 2.5 pair DBR diode chip with a PbTe absorber layer, as described in section 2.6.1. Unless otherwise stated they are performed for a design wavelength $\lambda_D = 5 \mu m$ and 120 K operating temperature. A wavelength independent absorption coefficient $\alpha = 5 \cdot 10^3 \text{ cm}^{-1}$ for the PbTe absorber is assumed. Apart from the absorber layer the absorbance is negligible small. The second mirror is a gold layer, with a reflectivity $R_2 = 99\%$. The cut-off wavelength is 5.35 μm for PbTe and 4.6 μm for $\text{Pb}_{0.99}\text{Sr}_{0.01}\text{Te}$. The width of the tunable range therefore is 0.75 μm , see section 2.3.1.

Quantum Efficiency

Within the cavity a standing wave is formed. The quantum efficiency is a function of wavelength [6]

$$\eta(\lambda) = \frac{1 + R_2 e^{-\alpha d}}{1 - 2\sqrt{R_1 R_2} e^{-\alpha d} \cos(2\beta L_{opt} + \psi_1 + \psi_2) + R_1 R_2 e^{-2\alpha d}} \times (1 - R_1)(1 - e^{-\alpha d}) \quad (2.1)$$

where

R_i	mirror reflectivities,
α	absorber layer absorption coefficient,
d	absorber layer thickness,
β	$= \frac{2\pi}{\lambda}$ propagation constant,
λ	wavelength,
L_{opt}	optical cavity length,
ψ_i	phase shift of reflected waves.

The resonance condition is fulfilled for wavelengths satisfying $2\beta L_{opt} + \psi_1 + \psi_2 = 2\pi m$, with the mode order $m = 1, 2, 3, \dots$. A change in cavity length of $\lambda_m/2$ yields a shift to the next lower or higher resonance mode. The phase shift on reflection at a metal mirror is $\psi_2 = \pi$. As discussed in section 2.2, the phase shift at the DBR ψ_1 depends on the deviation from the design wavelength.

The dependency of the quantum efficiency on wavelength and the optical characteristics of a RCED are shown in figure 2.2, calculated with equation (2.1) for two R_1 of 50 % and 95 %. The absorber thickness $d = 90$ nm. For comparison the maxi-

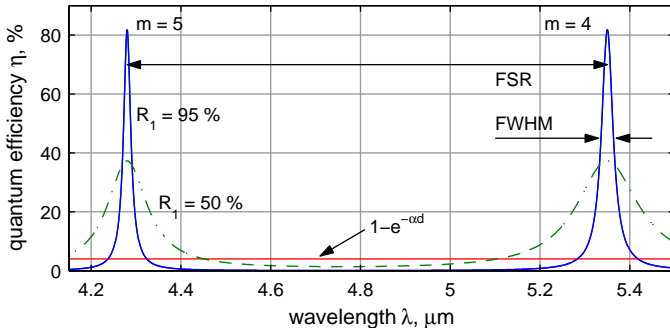


Figure 2.2: Calculated quantum efficiency of a RCED for different mirror reflectivities R_1 as a function of wavelength. Important characteristics are the peak width (FWHM) and the free spectral range (FSR). For comparison the wavelength independent quantum efficiency of an absorber layer with an equal thickness (90 nm) but without resonant enhancement is also shown.

imum quantum efficiency of an absorber with an equal thickness but without any resonant enhancement $1 - e^{-\alpha d}$ is shown as well. At the resonance modes it is surpassed many times over by the quantum efficiency of the RCED.

The maximum achievable quantum efficiency for the fulfilled resonance condition depends on the mirror reflectivities and the absorbance within the cavity. For a higher reflectivity R_2 it increases, while there is a optimum value for R_1 depending on the absorbance within the cavity. Generally with an increasing R_1 the absorbance has to be decreased. The optimal absorbance yielding maximum quantum efficiency is calculated with [6]

$$\alpha d = \frac{-1}{2} \ln \left(\frac{R_1}{R_2} \right). \quad (2.2)$$

This correlation is shown in figure 2.3 as a function of R_1 . For high mirror reflectivities the ideal absorbance decreases severely. In a real device this can be achieved easily by reducing the thickness of the absorber layer. However, if the thickness of the absorbing layer becomes to small, quantization effects would have to be considered. An active layer with absorbing quantum dots may be used to reduce the absorbance further.

FSR and FWHM

The free spectral range (FSR) is the distance between two neighboring resonance peaks. It can be derived from the resonance condition as

$$FSR = \lambda_m - \lambda_{m+1} = \frac{\lambda_m}{m + 1 - \frac{\psi_1}{2\pi} - \frac{\psi_2}{2\pi}}. \quad (2.3)$$

The FSR limits the maximum wavelength range over which single-mode tuning is possible. It decreases with higher mode order or increasing cavity length. Figure 2.4 shows the correlation of resonance peak wavelength, cavity length, and mode order. A change in cavity length of $\lambda_m/2$ yields a shift to the next lower or higher resonance mode, independent of the actual mode order. Therefore, with a change of cavity length of $\lambda_m/2$, any chosen resonance peak can be shifted over its corresponding

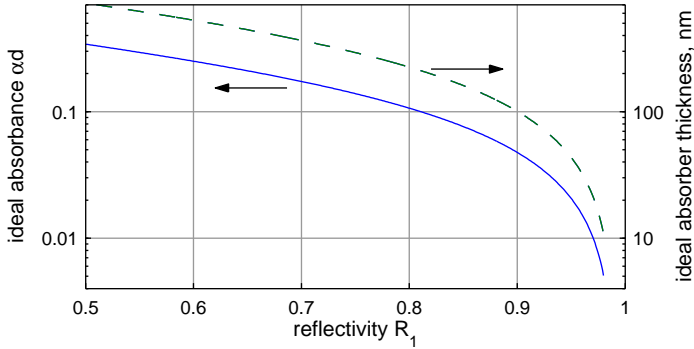


Figure 2.3: *The ideal absorbance within the cavity yielding maximum quantum efficiency, and the corresponding PbTe layer thickness as a function of R_1 . For high mirror reflectivities the ideal absorbance decreases severely.*

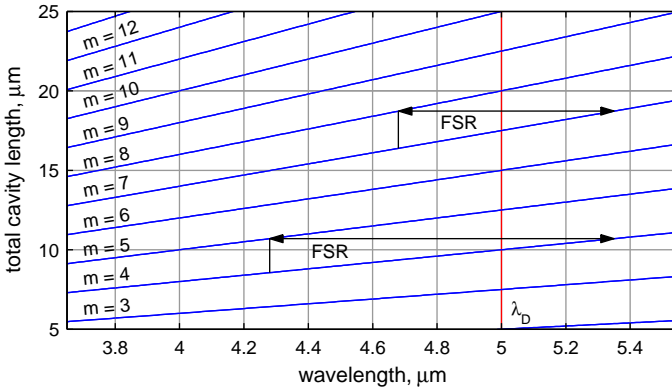


Figure 2.4: *Resonance peak wavelength for different mode orders as a function of cavity length. The wavelength range over which single-mode tuning is possible is limited by the distance of two neighboring peaks, the FSR. With increasing cavity length/higher mode order the FSR decreases.*

FSR. The FSR decreases with increasing cavity length/higher mode order.

The width at half maximum (FWHM) of each detection peak is given by [6]

$$FWHM = FSR \times \frac{1 - \sqrt{R_1 R_2} e^{-\alpha d}}{\pi (R_1 R_2)^{\frac{1}{4}} e^{-\alpha d/2}}. \quad (2.4)$$

The FWHM is reduced with higher mirror reflectivities and increasing resonance mode order.

FSR and FWHM are both reduced for increasing mode order. Hence there is a trade-off between a narrow peak width and the greatest possible tuning range. The dependency of FSR and FWHM on mode order is shown in figure 2.5. The absorber thickness is adapted with equation (2.2) for each R_1 to yield the maximum quantum efficiency. For increasing mirror reflectivities the FWHM becomes very narrow, well below 10 nm.

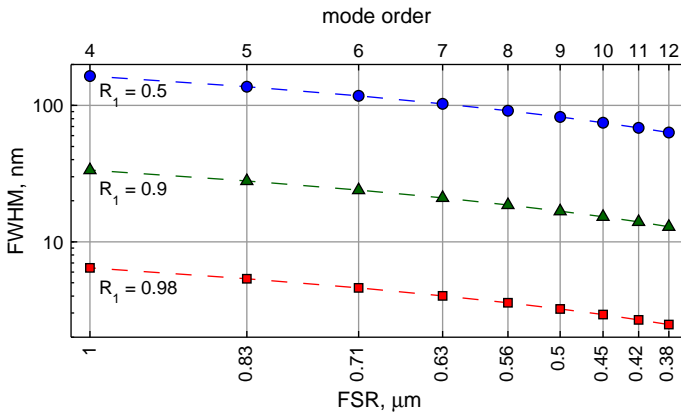


Figure 2.5: Change of FWHM with FSR/mode order for different mirror reflectivities R_1 . The absorber thickness is adapted for each R_1 to yield the maximum quantum efficiency.

Cavity Finesse

The quotient of FSR and FWHM is the finesse of the cavity. For an ideal RCED as described here the finesse is determined by the mirror reflectivities and the absorbance within the cavity. For a real device however, the theoretically possible finesse is degraded due to imperfections of the mirror planes and the measurement setup. As discussed in section 2.5, the FWHM of any detection peak is broadened as a consequence.

Effective Cavity Length

Due to the phase shift on reflection the cavity length is effectively larger than its optical length L_{opt} . For a metal mirror with a phase shift $\psi_2 = \pi$ the cavity is effectively increased by $\lambda/4$.

In the case of a DBR the phase shift depends on the wavelength of the incoming radiation, with no phase shift at the design wavelength. Figure 2.6 shows the calculated phase shift of the DBR as used in a RCED, and the resulting change in cavity length.

For the anticipated wavelength tuning range of $\pm 0.5 \mu\text{m}$ around the design wavelength, the change of the optical path length is less than $0.3 \mu\text{m}$. For small deviations around the design wavelength, it depends approximately linearly on the wavelength. As a consequence the shift of the resonance peak wavelength is slightly larger than expected from the movement of the movable top mirror.

Standing Wave Effect

Within the cavity a standing wave is formed. Figure 2.7 shows the distribution of the optical field within the cavity around the design wavelength. A detailed description of the diode chip is given in the following section 2.3.1. The calculation is performed with an absorber thickness of 20 nm, instead of the ideal value

of 12 nm. This thickness was chosen due to display reasons. For the ideal value the optical field is enhanced much more inside the cavity. Also shown are closeups of the active region for two different resonance conditions, for the external cavity lengths of 6.5 μm and 6.6 μm with the corresponding resonance wavelengths of 4.97 μm and 5.01 μm . Depending on cavity length, the standing wave is enhanced for one wavelength, while for the other wavelength it is much lower. This sharp change of intensity despite the relatively small change of cavity length is due to the narrow FWHM of the resonance peak.

The location of the absorber layer within the cavity is important for the quantum efficiency. It is generally placed at a maximum of the optical field. The peak position of the field maximum remains within the absorber, independent of mirror position and resonance wavelength.

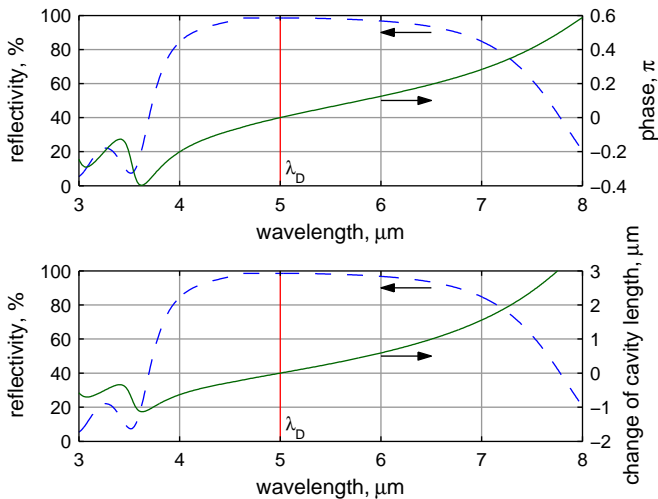


Figure 2.6: (top) Phase shift of the reflected wave at the innermost mirror interface as a function of wavelength and (bottom) change of cavity length due to this phase shift. For comparison the reflectivity of the 2.5 pair DBR stack is shown as well.

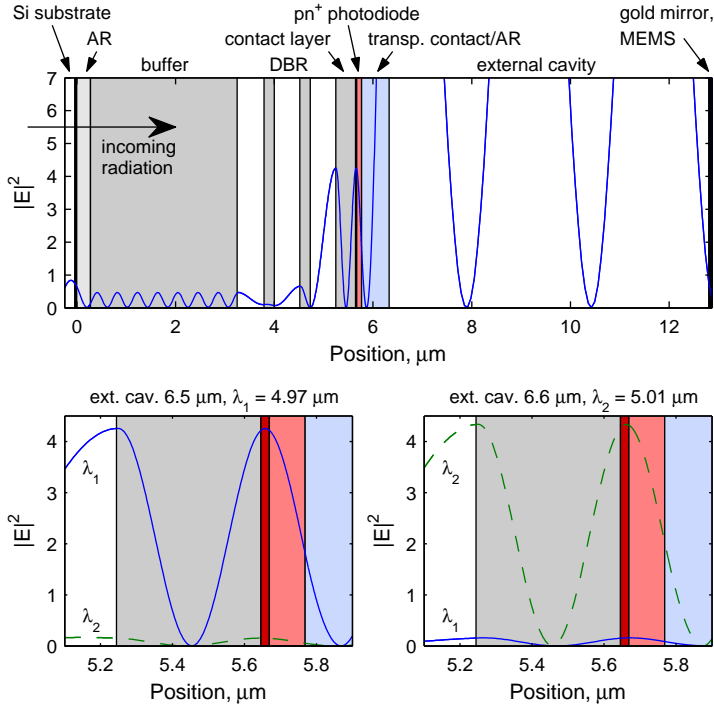


Figure 2.7: (top) Distribution of the E -field within the cavity as a function of position at the design wavelength. (bottom) Closeups of the active region for two different external cavity lengths of 6.5 μm and 6.6 μm with the corresponding resonance wavelengths of 4.97 μm and 5.01 μm . Depending on cavity length, the standing wave is enhanced for one wavelength, while for another it is much lower.

2.3 Diode Chip

2.3.1 Layer Stack Design

The schematics of the diode chip are shown in figure 2.8, using the example of a RCED with a 2.5 pair DBR and a PbTe absorber. Detailed schematics of the other realized setups are given in the corresponding sections 2.6.X for each device.

Incoming radiation passes through a $\lambda_D/4$ $\text{Pb}_{1-z}\text{Eu}_z\text{Te}$ AR layer as well as a $3\ \mu\text{m}$ thick $\text{Pb}_{1-x}\text{Sr}_x\text{Te}$ buffer layer before entering the cavity through the DBR. Generally $x \approx 1\%$ for the buffer and consecutive layers. To reduce the otherwise significant influence of the buffer layer on the reflectivity of the DBR the outer $\text{Pb}_{1-z}\text{Eu}_z\text{Te}$ AR layer is needed. Its Eu content $z \approx 8\%$ varies with the design wavelength and is chosen to yield the appropriate refractive index.

The DBR is composed of alternating $\text{EuTe}/\text{Pb}_{1-x}\text{Sr}_x\text{Te}$ layers. Due to the high refractive index contrast few pairs already yield a very high reflectivity over a broad wavelength range.

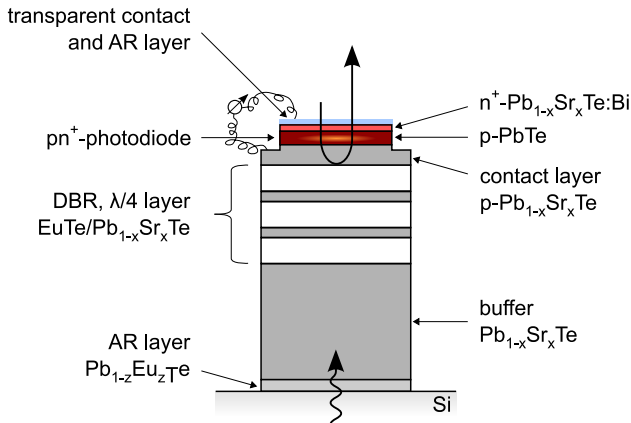


Figure 2.8: Schematics of the diode chip using the example of a RCED with a 2.5 pair BDR and a PbTe absorber.

The realized designs have 0.5 (a single layer EuTe), 1.5 and 2.5 layer pairs with corresponding reflectivities of 57 %, 92 % and 98.8 % for $\lambda_D = 5\mu m$ at 120 K.

The photodiode is a pn^+ heterojunction, with a p-type PbTe absorber layer followed by a 100 nm thick n^+ - $Pb_{1-x}Sr_xTe:Bi$. The ideal thickness of the absorber layer depends on the mirror reflectivities and its absorbance. The here shown example of a 2.5 pair DBR uses an absorber thickness of 30 nm. It was grown deliberately much thicker than the ideal value of 12 nm, in order to avoid quantization effects. For an 1.5 pair DBR the ideal thickness is ~ 100 nm. The electric resistance between diode and ohmic contact is too high for such thin layers. Hence an auxiliary transparent p-type $Pb_{1-x}Sr_xTe$ contact layer is necessary. The approximate band structure of the photodiode including contact layer is shown in figure 2.9. The thickness of the contact layer is adapted to place the absorber layer at a field maximum of the standing wave. In case of a 0.5 pair DBR with an absorber thickness of 300 nm the additional contact layer is not needed.

Due to alloying the bandgap of the $Pb_{1-x}Sr_xTe$ buffer layer (and of all consecutive $Pb_{1-x}Sr_xTe$ layers) is blue-shifted in respect to the absorber. Incoming radiation with wavelengths shorter than the cut-off of the buffer layer is effectively filtered before even entering the cavity. $Pb_{1-x}Sr_xTe$ is transparent for radiation with longer wavelengths. The cut-off wavelength of the buffer layer represents the shorter end of the wavelength range over which the RCED is sensitive. The longer wavelength end is given by the cut-off wavelength of the absorber layer.

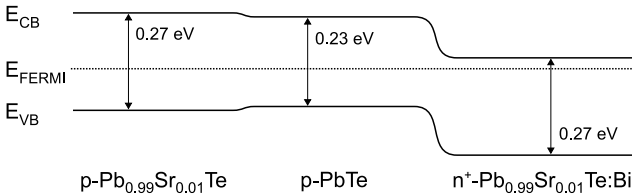


Figure 2.9: Band structure of the auxiliary PbSrTe contact layer and the p-PbTe n^+ -PbSrTe:Bi heterojunction.

For the appropriate alloy concentration x the width of this sensitive wavelength range is shorter than the FSR. Hence only one resonance peak is within the sensitive range, yielding single mode detection. Higher order resonance modes are filtered in the buffer layer, while lower mode orders are not detected since their wavelengths are longer than the cut-off wavelength of the absorber. At 120 K the cut-off wavelength is 4.6 μm for $\text{Pb}_{0.99}\text{Sr}_{0.01}\text{Te}$ and 5.35 μm for PbTe , at 180 K it is 4.2 μm and 4.76 μm , respectively. The width of the sensitive wavelength range therefore is 0.75 μm at 120 K and 0.44 μm at 180 K, see figure 2.10. For an effective cavity length shorter than 16 μm the FSR is larger than the sensitive range and the RCED operates with a single detection peak.

Structuring and electric contacting is done using standard photo-lithography techniques [11]. The etched diode mesas are octagonal with a diameter of 300 μm . Electroplated gold is used as ohmic contact next to the diode mesa. Depending on absorber thickness the p-PbTe is contacted directly, or via the auxiliary $\text{Pb}_{1-x}\text{Sr}_x\text{Te}$ contact layer. The n^+ layer is contacted with a transparent 100 nm thick Te layer deposited on top.

At the interface from diode to external cavity even a small reflectance creates a second internal cavity with its own resonance

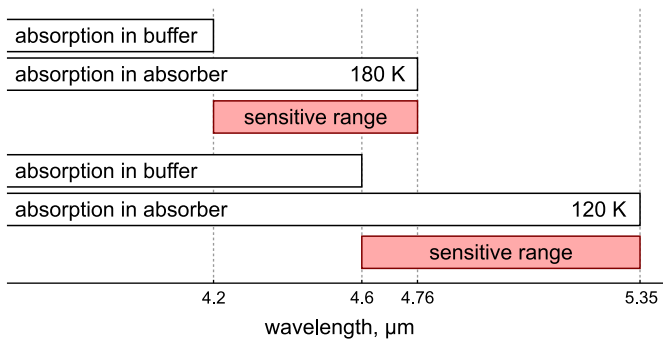


Figure 2.10: *The sensitive wavelength range of the RCED is defined by the cut-off wavelength of the buffer and the absorber layer. Its width decreases with increasing temperature.*

condition. This would yield a second very broad and not tunable peak as background signal. To reduce the unwanted effect a multilayer AR coating is used, with the transparent Te contact as first layer. ZnSe is used as material for its second layer. Its thickness is adapted depending on design wavelength and intended operation temperature to minimize reflectance. Figure 2.11 shows the calculated reflectivity of the Te ($n = 4.37$) and ZnSe ($n = 2.4$) layers combined with respect to deviation from design wavelength and temperature. The reflectivity is as low as 0.1 % at its minimum, and less than 2 % over the whole sensitive wavelength range.

By employing $\text{Pb}_{1-y}\text{Sr}_y\text{Te}$ as absorber layer the tunable range of the RCED can be shifted to shorter wavelengths. As a consequence the composition of all $\text{Pb}_{1-x}\text{Sr}_x\text{Te}$ layers, buffer, DBR and $n+$, has to be adapted, with alloy concentrations $x > y$. With the use of $\text{Pb}_{1-y}\text{Sn}_y\text{Te}$ as absorber material the tunable range can be shifted to longer wavelength. The buffer layer is then composed of $\text{Pb}_{1-x}\text{Sn}_x\text{Te}$ as well, here with alloy concentrations $x < y$. The DBR and contact layer are of pure PbTe.

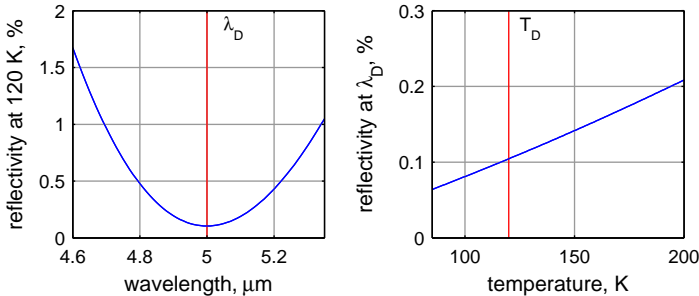


Figure 2.11: Calculated reflectivity of a multilayer Te/ZnSe AR coating as a function of deviation from (left) design wavelength and (right) intended operation temperature. It is well below 2 % for most of the tunable wavelength range.

2.3.2 High Sensitivity of Thin Photodiodes

For IV–VI materials there are two noise mechanisms limiting the theoretical possible performance [75]. The diffusion limit is the ultimate limit for every photodiode. It is determined by the Auger lifetime, which is very long for lead–salts. However, shorter lifetimes are common due to Shockley–Read (SR) recombination of carriers at defects in the depletion region. SR generally dominates at lower temperatures, while at higher temperatures Auger recombination is more important.

Diffusion Limit

For a thick and abrupt pn^+ photodiode without surface recombination, the diffusion limit is given by [75]

$$R_0 A_D = \frac{k_b T}{q^2} \frac{N_a}{n_i^2} \frac{\tau_e}{\sqrt{D\tau_e}}, \quad (2.5)$$

where

T	temperature,
k_b	Boltzmann constant,
q	electron charge,
N_a	acceptor density,
n_i	intrinsic carrier density,
τ_e	electron lifetime,
L_e	$= \sqrt{D\tau_e}$ electron diffusion length,
D	diffusion coefficient.

The strong temperature dependence is mainly caused by $n_i^{-2} \propto e^{E_g/kT}$, where E_g is the band gap energy. τ_e is limited by Auger recombination and depends on N_a , which is in the range of 10^{17} cm^{-3} for the discussed devices. The dependence on N_a is canceled in equation (2.5), thus making $R_0 A_D$ independent of the acceptor density.

For very thin diodes the carrier diffusion length is limited by the thickness d of the layer. L_e can then be replaced by d

$$R_0 A_D = \frac{k_b T}{q^2} \frac{N_a \tau_e}{n_i^2 d}. \quad (2.6)$$

Compared to a bulk absorber layer the sensitivity increases by L_e/d . In the case of a 0.3 μm thin PbTe absorber layer, this yields an about 40-fold increase of the diffusion limit.

Generation–Recombination

Due to generation and recombination of carriers at defects in the depletion region, carrier lifetimes τ_{SR} can be shorter than the Auger lifetime. The sensitivity is then [75]

$$R_0 A_{SR} = \frac{2k_b T}{q} \frac{\ln\left(\frac{N_a N_d}{n_i^2}\right)}{n_i} \frac{\tau_{SR}}{w}, \quad (2.7)$$

where

- N_d donor density,
- τ_{SR} Shockley–Read lifetime,
- w width of the depletion region.

In case of a thin absorber layer on top of a insulating EuTe layer the width of the depletion region equals the thickness of the absorber layer.

Experimental Results

Both diffusion limit and limit due to finite Shockley–Read carrier lifetime are shown in figure 2.12. The diffusion limit $R_0 A_D$ is calculated using equation (2.5) for a thick absorber, and (2.6) for a 0.3 μm thin absorber. The $R_0 A_{SR}$ is calculated using equation (2.7) for three different carrier lifetimes τ_{SR} of 1 ns, 10 ns and 100 ns.

The experimental R_0A of a RCED with a $0.3\ \mu\text{m}$ thick PbTe absorber are also shown in figure 2.12, measured for various discrete temperatures. They are derived from fitted unilluminated current–voltage curves and corrected for series resistances. For temperatures above 200 K the experimental values are better than those for an optimized bulk diode, but below the theoretical limit for a thin absorber. Towards lower temperatures the slope of the measured values is about half of the one of the diffusion limit. This indicates that the diodes are limited by Shockley–Read recombination at defects in the depletion region. Additionally the ideality factors n^* of the measured current–voltage curves changes from $n^* = 1$ indicating band to band recombination to $n^* \approx 2$ for SR recombination towards lower

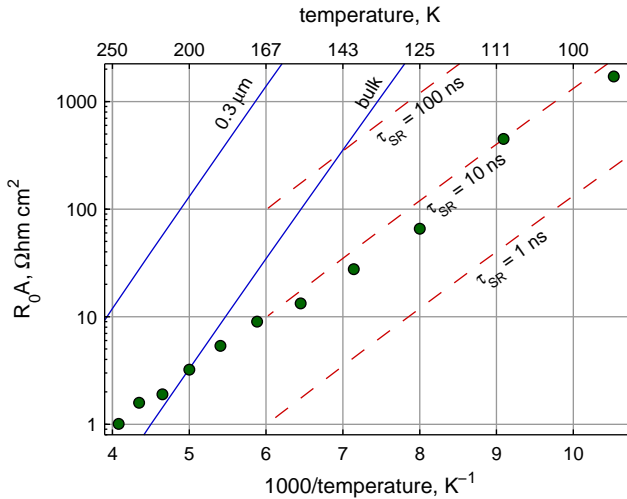


Figure 2.12: Measured R_0A product and theoretical limits as function of inverse temperature. The diffusion limit R_0A_D is calculated for a thick and a $0.3\ \mu\text{m}$ thin absorber (solid). The Shockley–Read R_0A_{SR} is calculated for carrier lifetimes of 1 ns, 10 ns and 100 ns (dashed). For temperatures above 200 K the experimental values of a $0.3\ \mu\text{m}$ thin PbTe absorber (dots) are above the theoretical limit of a comparable conventional bulk absorber layer [own publications, article 3].

temperatures. For temperatures below 200 K the slope of experimental R_0A is determined by a lifetime $\tau_{SR} = 10 \text{ ns}$.

The measured Shockley–Read lifetimes in a thin absorber are much higher when compared to PbTe bulk photodiodes fabricated previously on Si substrate [72,76]. There a rough agreement of the Shockley–Read lifetimes with the diffusion lengths was found for thick PbTe absorber layers. The diffusion lengths were limited by the mean distance between threading dislocations crossing the active region. However, the observed lifetimes of thin diodes are significantly higher, even though it is more difficult to obtain low dislocation densities in not exactly lattice matched very thin layers.

One may conclude that this is due to the limited thickness volume of the active device part. In the smaller volume less noise due to Shockley–Read generation and recombination of charge carriers occurs. By thinning the base p–type region of the photodiode to a thickness smaller than the minority carrier diffusion length, the corresponding R_0A product increases, provided that the noise current is diffusion limited and the back contact is characterized by a low recombination rate [77,78]. Such a correlation between noise and layer thickness was found experimentally: for thin layers the R_0A product increases with decreasing layer thickness [own publications, article 10]. The minimum feasible thickness of the layer is however limited. With a decreasing layer thickness the series resistance increases, resulting in a poorer electric contacting of the diode.

2.4 MEMS Micro–mirror

The top mirror of the RCED is realized using a vertically movable MEMS micro–mirror. It is fabricated by the Center of Mechanics at ETH Zurich [74]. A detailed description of the different mirror setups and the fabrication process can be found elsewhere [79].

The micro–mirror is essentially a silicon membrane suspended on thin arms and coated with a gold layer for high reflectivity. It

can be moved by electrostatic forces. The suspension geometry defines the elastic constant and thus the applied voltage needed for a certain displacement. Two setups have been realized and used in a RCED, see figure 2.13 and table 2.1 for a comparison.

In the parallel plate setup the mirror membrane itself acts as one of the actuation electrodes. Four aluminum pads on the glass substrate are the opposing electrodes. For opposite charges applied the membrane is attracted, thus increasing the cavity length. For equal charges it is pushed away, thus decreasing the cavity length. The displacement depends approximately quadratically on the applied voltage. The maximum displacement is limited by irreversible mechanical deformation and pull-in. For both realized setups it is $\sim 3 \mu\text{m}$ in either direction. For the targeted wavelengths ($3\text{--}8 \mu\text{m}$) this is more than sufficient to yield a shift of the current resonance mode order to the next one. Due to internal stress the membrane is curved away from the cavity with a typical radius of 0.2 m . This convex curvature of the mirror can be reduced or even inverted with a thin layer of Cr, which is deposited on the membrane before the reflective gold layer.

The second setup is based on a comb-drive actuator: two opposing combs with alternating fingers of two different heights, one attached to the movable mirror and the other one fixed. The actuation mechanism is based on the asymmetry of the electric field between the combs. With increasing voltage the cavity length is decreased, with a total mirror travel of $\sim 3 \mu\text{m}$. For the comb-drive actuated version the mirror plate can be fabricated much stiffer. Deformations due to internal stress are then mainly induced into the suspension instead of the mirror plate. Therefore the mirror surface curvature is drastically reduced, with a radius of curvature of $1\text{--}2 \text{ m}$ towards the cavity (concave).

The characteristics of the two actuation designs differ due to fabrication process and suspension geometry. The characteristics of the setup using the comb-drive actuation are superior. The influence of slight shortcomings of the mirror plane on the FWHM of a resonant peak is discussed in section 2.5.

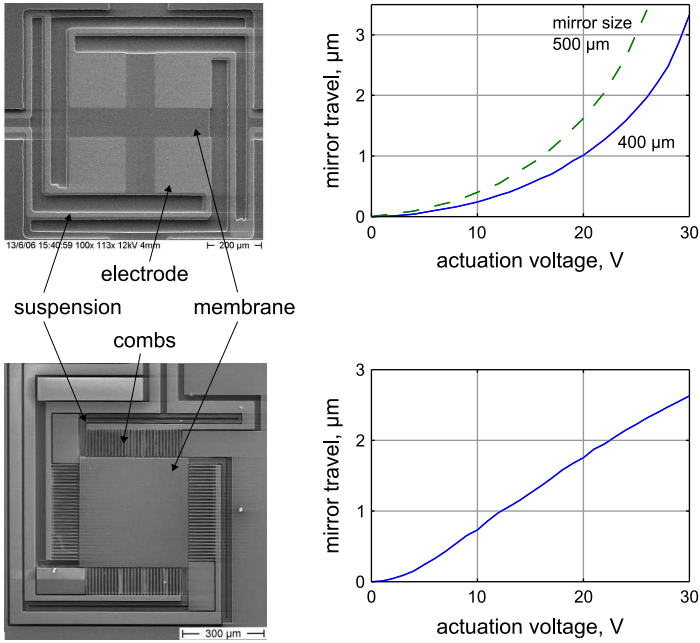


Figure 2.13: Top view of a MEMS micro-mirror in (top) parallel plate setup and with (bottom) comb-drive actuation. The vertical displacement of the mirror membrane depends on geometry and actuation voltage.

	parallel plate	comb-drive
change of cavity length for opposite charges	increasing	decreasing
radius of curvature [m]	(convex) 0.2	(concave) 1 – 2
initial non-parallelism [°]	< 0.05	0.06
axes tiltable by actuation	x-direction	x-, y-direction
surface roughness, rms [nm]	5	2

Table 2.1: Comparison of the characteristics of the MEMS micro-mirrors with parallel plate and comb-drive actuation.

By applying different actuation voltages to the individual electrodes the mirror membrane can be tilted, in both axes for the comb-drive actuated version. With the parallel plate setup the electrodes are only addressable pairwise at this time, making the mirror tiltable in one axis. A reversible total angle variation of more than 0.2° has been achieved. This is much greater than the initial non-parallelism of the mirror membrane due to internal stress after processing. Additionally it allows to correct a possible (parallel) misalignment of the MEMS chip in respect to the lower diode chip. An elevation difference caused by the spacer layer of up to $30\ \mu\text{m}$ could be compensated, far above the usually encountered thickness variations in such thin films very well below $1\ \mu\text{m}$. Figure 2.14 shows a white light interferometer 3D image of a tilted micro-mirror in parallel plate setup. The membrane is irreversibly tilted, with a $10\ \mu\text{m}$ elevation increase from front to back.

The MEMS micro-mirrors have mechanical resonances in the vertical direction at $\sim 10\ \text{kHz}$. These mechanical resonance modes depend strongly on the geometry of the mirror and the suspensions, whereby the thickness of the suspensions has a major influence. The resonance frequencies can be designed to be

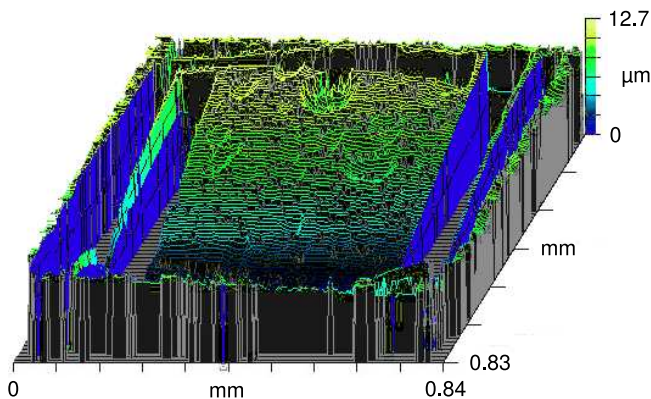


Figure 2.14: White light interferogram of a tilted MEMS micro-mirror in parallel plate design. The membrane is tilted, with a $10\ \mu\text{m}$ elevation increase from front to back.

below 1 kHz for a vertical parallel mirror movement. The RCED may then be operated in such a mechanical resonant mode, thus allowing kHz scanning of the entire tunable range.

2.5 Practical Limitations

In accordance with section 2.2, the following calculations are performed for a design wavelength $\lambda_D = 5 \mu m$ and 120 K operation temperature. The diode chip design as described in section 2.3.1 is used, with a 2.5 pair DBR and a PbTe absorber.

Cavity Finesse

As stated before, the finesse of the cavity is the quotient of FSR and FWHM. The calculated value F_t of an ideal device is degraded due to imperfections of the mirror plates and the measurement setup [80, 81]. The consequence is a broadened detection peak.

There are three defects of the perfect mirror plane contributing to the defect finesse, see figure 2.15: the curvature t_C of the mirror plane

$$F_C = \frac{\lambda}{2t_C},$$

the roughness of the mirror surface, with the root mean square of the surface roughness t_{RMS}

$$F_R = \frac{\lambda}{4.7t_{RMS}},$$

and the deviation t_P from perfectly parallel aligned mirror planes

$$F_P = \frac{\lambda}{\sqrt{3}t_P}.$$

Apart from the device, the imperfect measurement setup adds to the peak broadening as well. The incoming radiation is

not a perfectly collimated beam as assumed in all previous calculations. It has an opening angle depending on the aperture of the FTIR. Additionally its incidence is not exactly perpendicular. For a thin absorber with its low absorption this results in an outward traveling of the reflected rays within the device. This aperture finesse

$$F_A = \frac{2\pi}{m\Omega}$$

depends on the mode order m and the solid angle of the incident light $\Omega = S/r^2$.

The theoretical, defect and aperture finesse together yield the effective finesse

$$F_{eff} = \left(\frac{1}{F_t^2} + \frac{1}{F_C^2} + \frac{1}{F_R^2} + \frac{1}{F_P^2} + \frac{1}{F_A^2} \right)^{-\frac{1}{2}}. \quad (2.8)$$

With the relation between finesse, FSR and FWHM the peak broadening may be calculated as function of FSR. Figure 2.16 shows the theoretical FWHM for two typical devices, with (top) a 2.5 and (bottom) a 0.5 pair DBR, as a function of mode order. Due to the lower mirror reflectivity the FWHM of the RCED using a 0.5 pair DBR is much higher by default. Also shown are the individual contributions of each cavity defect adding to the theoretical FWHM. The resulting effective FWHM is calculated with equation (2.8).

The calculations are performed for typical values of a MEMS mirror in parallel plate setup, see section 2.4. The deviation

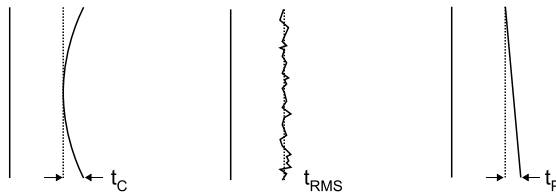


Figure 2.15: *Mirror plane defects contributing to the defect finesse: curvature, surface roughness, and deviation from parallelism.*

from perfect parallelism is assumed to be $t_P = 150$ nm, the curvature radius of 0.2 m yields $t_C = 60$ nm, and the surface roughness is $t_{RMS} = 5$ nm. The opening angle of the incoming beam depends on the focal aperture setting of the measurement

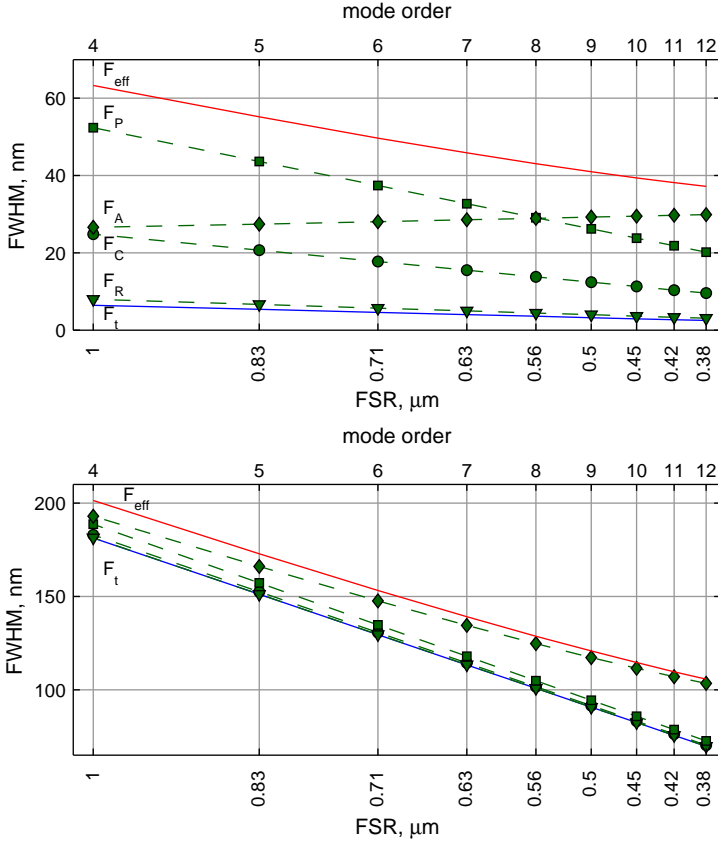


Figure 2.16: *FWHM of a RCED with (top) a 2.5 pair DBR and (bottom) a 0.5 pair DBR as function of mode order. The theoretical possible value F_t is degraded due to the different cavity defects. The influence of each cavity defect on FWHM is shown individually. The total of all defects yields the effective finesse F_{eff} . See text for details.*

FTIR. Since the exact correlation is unknown, values are estimated from the exit window size and the different aperture settings. The calculations in figure 2.16 are performed for (top) an opening angle of 13° , which yields $\Omega = 0.04$, and (bottom) 20° , which yields $\Omega = 0.1$,

The realized devices typically detect the mode order 7 and above. The influence of the measurement setup, the opening cone of the incident beam, is the dominant contribution on peak broadening. Its influence increases with mode order, defining the minimum measurable FWHM. Concerning the cavity defects, the influence of mirror plate parallelism is dominating. The influence of the mirror plane curvature is much less pronounced, while surface roughness can be neglected. Contrary to the contribution caused by the aperture angle, the effects from cavity defects decreases with increasing mode order.

The peak broadening is especially important for devices with a 2.5 pair DBR. Here the theoretical possible FWHM may be degraded by a factor of 10. For devices with a lower mirror reflectivity R_1 the absolute degradation is of the same order, however the relative impact is much lower.

Wavelength Dependent Absorption Coefficient

In all previous calculations the absorption coefficient of the absorbing PbTe layer was assumed constant. This is however not the case, since it rather changes dramatically with wavelength. Over the tunable range the absorption coefficient of the absorber layer increases from 0 at its cut-off wavelength up to 10^4 cm^{-1} at the cut-off wavelength of the buffer layer. Hence the absorbance within the cavity is not ideal for all wavelengths except the design wavelength. As a consequence the maximum quantum efficiency and the FWHM vary over the tunable wavelength range. Figure 2.17 shows the calculated quantum efficiency vs wavelength over the whole tunable range. The additional x-axes show the varying absorbance as well as the calculated FWHM. The PbTe absorber thickness used in the calculation is 30 nm. Its ideal thickness however is 12 nm, with $\alpha d = 0.005$ for the

design wavelength. For that case, the increase of quantum efficiency is less steep close to the PbTe cut-off wavelength.

The $\text{Pb}_{0.99}\text{Sr}_{0.01}\text{Te}$ buffer layer is used as a filter for wavelengths shorter than the tunable range. Figure 2.18 shows its transmission for two thicknesses. Close to its cut-off wavelength a significant portion of the incoming radiation is transmitted. This holds even for a much thicker buffer than the typically used $3\ \mu\text{m}$. As a consequence, the short wavelength edge of the tunable range is not sharp. The detected signal rather fades out towards shorter wavelengths, as the transmission through the buffer decreases due to the increasing absorption coefficient.

As a consequence of these two effects, the maximum achievable quantum efficiency varies over the sensitive wavelength range. Both edges are blurred, and at the design wavelength a maximum occurs. For a narrow sensitivity range this effect is more pronounced. In case of a wider sensitive wavelength range a plateau with high quantum efficiency is observed.

Beam Diameter and Diode Mesa

During the resonance calculations it was assumed, that all incoming radiation contributes uniformly to the interference in the cavity. In a real device, this presumption is synonymous to incoming radiation being limited to the diode mesa area. However, for the realized devices no optical shielding was used and the diameter of the incoming beam is larger than the diode mesa. The radiation passing the chip next to the mesa contributes to a not tunable background signal, provided it is absorbed. There the resonance condition is completely different compared to the condition for radiation passing the diode chip through the mesa.

Whether radiation passing the chip next to the mesa is absorbed depends on the setup of the photodiode. In case of the RCED setup described in section 2.3.1 the absorber layer is very thin and thus completely removed (apart from the diode mesa) during processing. The contact layer underneath is not absorbing, hence there is no influence of the radiation passing the chip next to the mesa on the detected signal. However, for a RCED

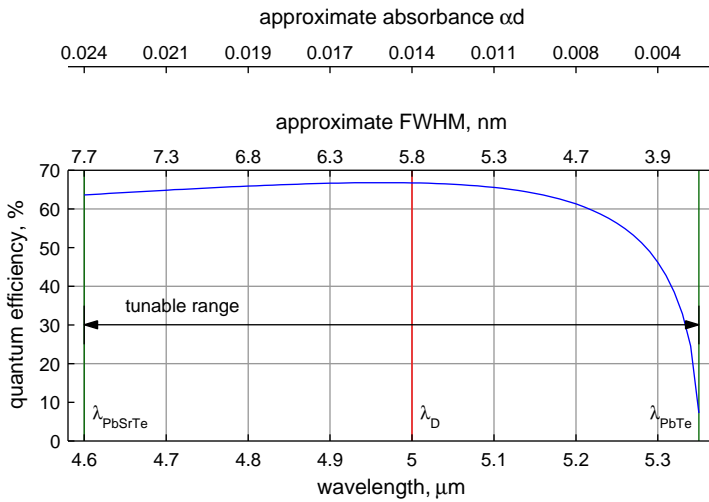


Figure 2.17: Quantum efficiency as a function of wavelength. The dependency is due to the increasing absorption coefficient from the cut-off wavelength towards shorter wavelengths. As a further consequence, the FWHM also changes with wavelength.

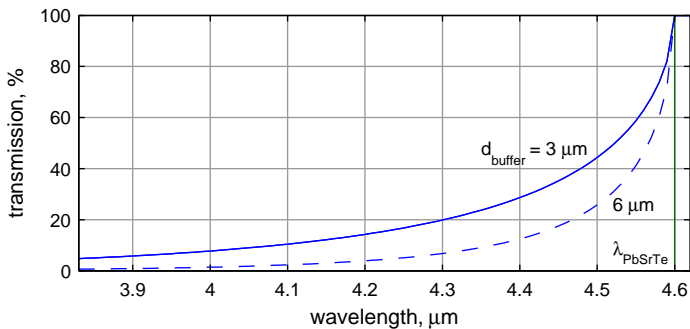


Figure 2.18: Transmission through a 3 μm and a 6 μm thick $\text{Pb}_{0.99}\text{Sr}_{0.01}\text{Te}$ layer as a function of wavelength. Close to the cut-off wavelength the transmission intensity is substantial.

setup with a 0.5 pair DBR the absorber layer is thicker and not completely removed. The additional signal is not tunable. With changing cavity length, the resonances are shifted over this not tunable background signal.

2.6 Tunable RCED Devices

Table 2.2 summarizes the different configurations of the diode chips employed. Two RCED using a PbTe absorber have been realized. For the device with the 2.5 pair DBR the finesse of the cavity is very high, resulting in a narrow FWHM (35 nm) of the resonance peak. The second device has a DBR with 0.5 pairs and is optimized for a high operation temperatures (> 240 K). Due to the temperature dependence of the bandgap its sensitive range is shifted towards shorter wavelengths. Two more RCED use chemical tuning to reach shorter or longer wavelengths, with the ternary alloys PbSrTe and PbSnTe as absorbing layers, respectively.

Typically a MEMS micro-mirror in parallel plate actuation setup is used. A RCED using the comb-drive actuation mechanism has been realized as well [79].

absorber	buffer	DBR [pairs]	λ_C [μm]
PbTe	$\text{Pb}_{0.983}\text{Sr}_{0.017}\text{Te}$	2.5	5.0
PbTe	$\text{Pb}_{0.965}\text{Sr}_{0.035}\text{Te}$	0.5	3.6–4.5
$\text{Pb}_{0.98}\text{Sr}_{0.02}\text{Te}$	$\text{Pb}_{0.965}\text{Sr}_{0.035}\text{Te}$	0.5	3.7
$\text{Pb}_{0.94}\text{Sn}_{0.06}\text{Te}$	$\text{Pb}_{0.885}\text{Sn}_{0.115}\text{Te}$	1.5	7.1

Table 2.2: Realized RCED setups with the center wavelength λ_C of the sensitive wavelength range.

2.6.1 PbTe RCED

PbTe RCED with low FWHM

Figure 2.19 shows the setup of the realized PbTe RCED designed for a narrow resonance peak width. The structure is discussed in detail in section 2.3.1.

In figure 2.20 individual measured quantum efficiency curves are shown. The detected resonance peak of mode order $m = 10$ is shifted depending on mirror position. For an actuation with -53.5 V (equal charges applied to the electrodes) the external cavity length is $16 \mu\text{m}$. It is increased to $18 \mu\text{m}$ for an actuation with $+32$ V (opposite charges applied). At the same time the resonance peak wavelength is shifted from $\sim 4.3 \mu\text{m}$ up to $\sim 4.7 \mu\text{m}$. The quantum efficiency has a maximum around the center wavelength, as explained in section 2.5. The absolute values for the quantum efficiency were obtained from a calibration mea-

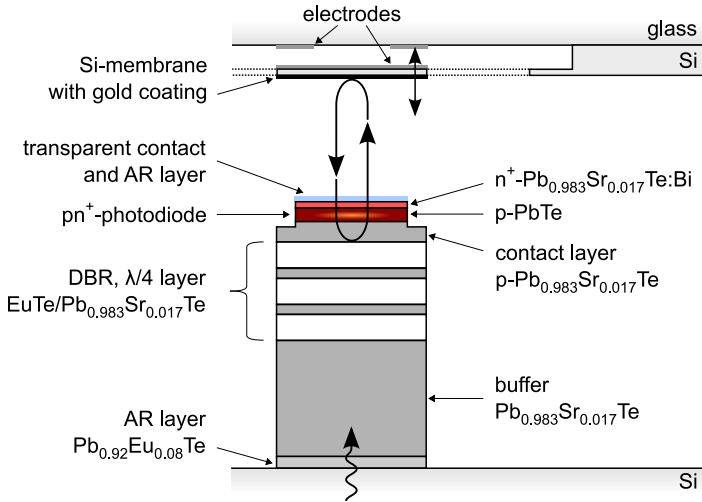


Figure 2.19: Schematics of a RCED using a PbTe–PbSrTe heterojunction as photodiode. Due to the high reflectivity of the 2.5 pair DBR it offers a narrow FWHM.

surement with a 500 K blackbody radiator using a monolithic RCED as reference device [9].

For a FTIR aperture diameter of 2 mm the FWHM of the resonance peak is 35 nm, $\Delta\lambda/\lambda < 0.8\%$. The background correction does reduce the FWHM slightly, since the half maximum is shifted upwards relative to the spectrum. The signal-to-noise contrast is 5:1 for the uncorrected measurement. For a FTIR aperture diameter of 4 mm the FWHM is increased significantly to 43 nm.

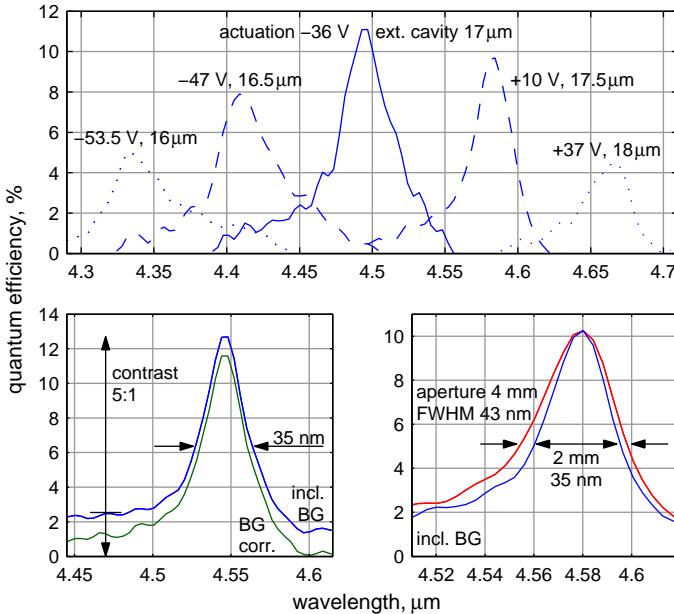


Figure 2.20: (top) Background corrected quantum efficiency for different actuation voltages as a function of wavelength. With the change of cavity length the resonance peak is shifted. (left) Comparison of the resonance peak as measured, and background corrected. The FWHM is 35 nm, $\Delta\lambda/\lambda < 0.8\%$. (right) With a larger aperture setting of the measurement FTIR the peak broadens considerably.

The FWHM of the resonance peak corresponds well with the calculated value of < 40 nm in section 2.5. As discussed there, the theoretical finesse of the cavity is degraded due to cavity defects, resulting in a broadened FWHM. This degradation has two causes: For one thing the mirror planes are not perfect. There are the deviation from parallelism of mirror planes, the curvature of the MEMS mirror membrane and dispersion due to surface roughness. For another thing the incoming measurement beam is not perfectly collimated. The exact correlation between aperture setting and opening angle of the radiation is however unknown and a quantitative comparison therefore difficult.

As discussed previously, the influence of the measurement setup and the mirror parallelism are dominating. There are different improvements possible for a further reduced FWHM. For one thing the incoming beam can be collimated. This can be done by a plano-convex high refractive index material just beneath the Si substrate, acting as a collimating lens. For another thing the cavity finesse can be improved. With the currently used MEMS mirrors in parallel plate setup, a correction of parallelism is only possible in one direction. Hence a perfect correction of an arbitrary tilt is not possible. With the use of a comb-drive actuated mirror, the initial misalignment is expected to be significantly reduced.

Figure 2.21 shows the Color-coded quantum efficiency calculated for different cavity lengths, and the experimentally determined curves for different actuation voltages, as measured and with background correction (2 mm aperture). The tunable wavelength range is ~ 0.4 μm wide, extending from 4.3 μm to 4.7 μm . The maximum mirror travel is 4.5 μm . The minimum external cavity length is 15.8 μm , for an identical potential of 57 V applied to the opposing electrodes. The additional optical path length in matter is 4.2 μm . The detected signal originates from mode orders 10 and 11. The resonance mode 10 is single-mode over the whole tunable wavelength range. The short wavelength end of the tunable range at 4.3 μm corresponds very well with a Sr concentration of $x = 1.7\%$ in the buffer layer (100 K operation temperature). The long wavelength end of the tunable range at 4.7 μm however is contradictory to the cut-off wavelength of

PbTe (5.5 μm at 100 K).

The absorber layer is not thin enough for quantization effects to cause such a strong shift of the cut-off wavelength. This significant shift can be best explained by absorption in a layer with $\sim 1\%$ Sr content. However, the not tunable background signal of the RCED extended well up to the expected PbTe cut-off wavelength. The possibility of Sr diffusion from the auxiliary contact layer into the absorber during growth can therefore be ruled out. Absorption in the auxiliary contact layer can be ruled

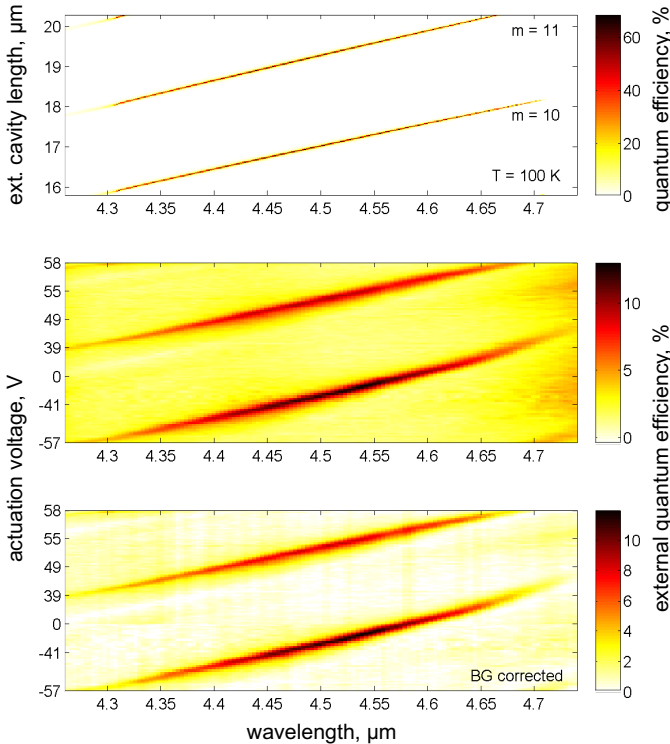


Figure 2.21: (top) Color-coded quantum efficiency of a PbTe RCED calculated for different cavity lengths, and measured curves for different actuation voltages (middle) as measured and (bottom) background corrected.

out as well. Due to the thickness of this layer the absorbance would be too high, resulting in a much lower peak quantum efficiency and at the same time a much broader FWHM. One possible explanation is the absorption mainly occurring in the n^+ -layer, instead of the p-absorber. Such a junction migration has been reported for PbTe-PbSnTe heterostructure diodes [82]. A precondition is a lower than anticipated Sr content in the n^+ -layer. For the calculation a Sr content of $\sim 1\%$ in the absorber layer was assumed.

PbTe RCED at high T

Figure 2.22 shows the RCED setup for high operation temperatures. The 300 nm thick PbTe absorber layer is highly sensitive, as described in section 2.3.2. Its thickness constitutes a compromise between an even thinner layer for less noise on the one side, and a greater layer thickness for improved electric conductivity to the ohmic contact and an optimized absorbance within the cavity yielding maximum quantum efficiency on the other side. The use of an additional $\text{Pb}_{1-x}\text{Sr}_x\text{Te}$ contact layer as in the RCED described above is not useful in this case. According to Hall measurements, the ternary alloy has an inferior crystal quality than pure PbTe. Hence, instead of improving the sensitivity at the intended high operation temperatures, such a contact layer would be counter-productive: the generated noise would be greater than of an even thicker PbTe absorber, while the conductivity would be worse.

Figure 2.23 shows the color-coded response curves for different actuation voltages measured at 240 K, 215 K, 175 K, 135 K, and 95 K (background corrected, 8 mm aperture). Due to the large bandgap (high Sr content of $x = 3.5\%$) in the buffer layer the sensitive wavelength range is very broad, resulting in a multi-mode spectrum regardless of the cavity length. With increasing temperature the sensitive wavelength range is shifted towards shorter wavelengths. At the same time it becomes less broad, since the cut-off wavelengths of buffer and absorber layer do not shift uniformly. At 95 K the mode orders 10 to 15 are detected, and at 240 K the mode orders 13 to 18. With higher

mode orders the distance between the resonances is reduced. The shortest external cavity length is $22\ \mu\text{m}$, with an additional $\sim 3.9\ \mu\text{m}$ in matter. The optical length in matter changes slightly with temperature, due to a decrease of the refractive index of lead-salts. This is seen as a slight shift of the respective mode order towards shorter wavelengths with increasing temperature. The maximum mirror travel is $2.5\ \mu\text{m}$ for a maximum actuation voltage of $76\ \text{V}$. The anomaly in the measured response curves at $\sim 4.25\ \mu\text{m}$ is caused by CO_2 absorption in the beam path of the measurement FTIR.

When operating at $> 200\ \text{K}$, the device can be cooled thermoelectrically. Even higher operation temperatures are achievable with an increased crystal quality.

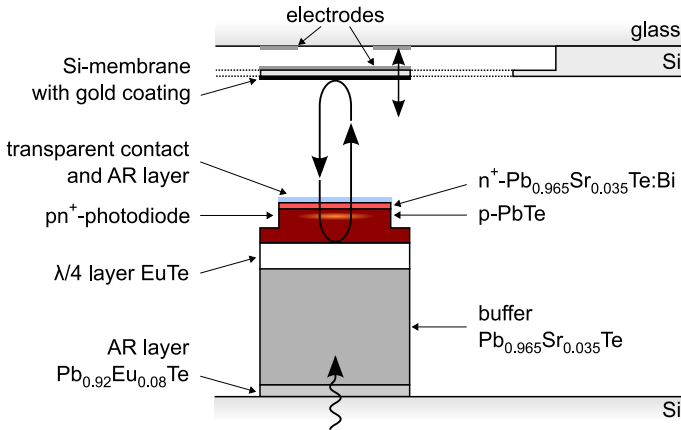


Figure 2.22: Schematics of a RCED using a PbTe-PbSrTe heterojunction as photodiode. It is optimized for operation temperatures up to $> 240\ \text{K}$.

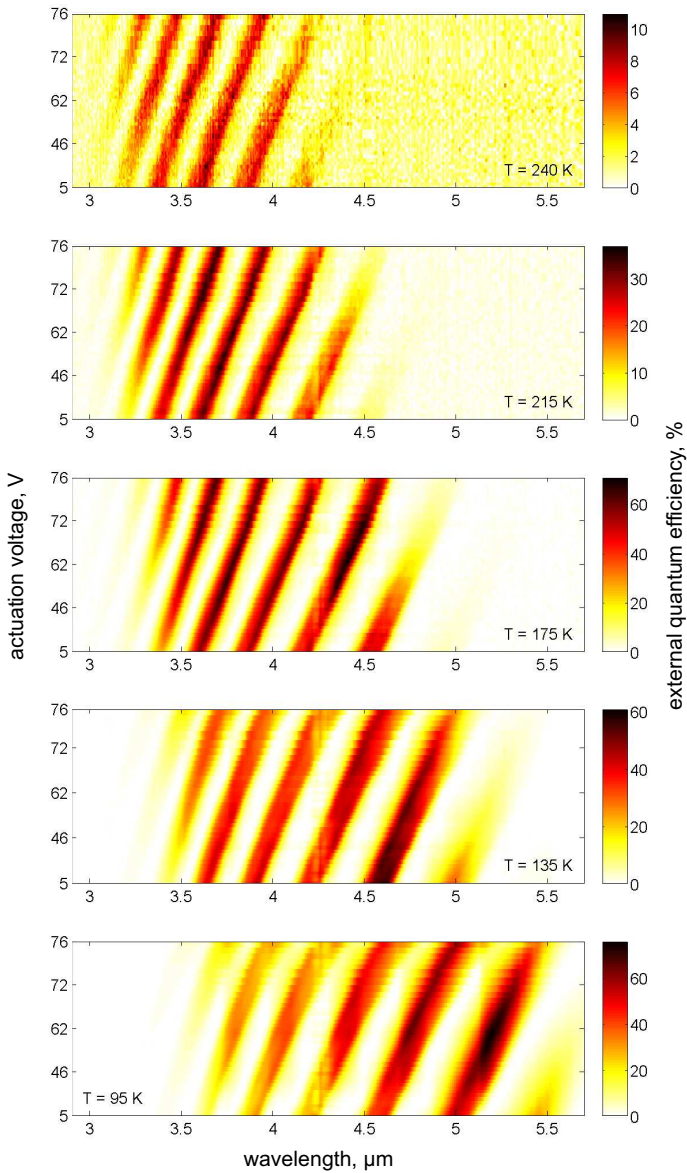


Figure 2.23: Color-coded quantum efficiency of a PbTe RCED for different actuation voltages measured at 240 K, 215 K, 175 K, 135 K, and 95 K (BG corrected).

2.6.2 PbSrTe RCED for Shorter Wavelengths

With increasing Sr content the cut-off wavelength of PbSrTe is shifted towards shorter wavelengths. Figure 2.24 shows the schematics of a RCED using a p-Pb_{1-y}Sr_yTe/n⁺-Pb_{1-x}Sr_xTe:Bi heterojunction as photodiode. Due to the blue-shifted bandgap the composition of the Pb_{1-x}Sr_xTe buffer layer has to be adapted as well, with $x > y$. The lower DBR is a single $\lambda/4$ EuTe layer.

Figure 2.25 shows the color-coded quantum efficiency calculated for different cavity lengths, and the measured response curves for different actuation voltages (background corrected, 8 mm aperture). The calculation is performed for 120 K with Sr concentrations of $x = 3.5\%$ in the buffer and $y = 2\%$ in the absorber layer. The tunable region is $\sim 0.5\ \mu\text{m}$ wide between $3.5\ \mu\text{m}$ and $4\ \mu\text{m}$. The mode orders 7 to 9 are detected, over a wide range single mode. The shortest external cavity length is $7.6\ \mu\text{m}$, with an additional $4.3\ \mu\text{m}$ in matter. The maximum mirror travel is $3.5\ \mu\text{m}$ for a maximum actuation voltage of 59 V. The FWHM of the peak is $\sim 150\ \text{nm}$, $\Delta\lambda/\lambda = 4\%$. This again corresponds well with the values calculated for a RCED

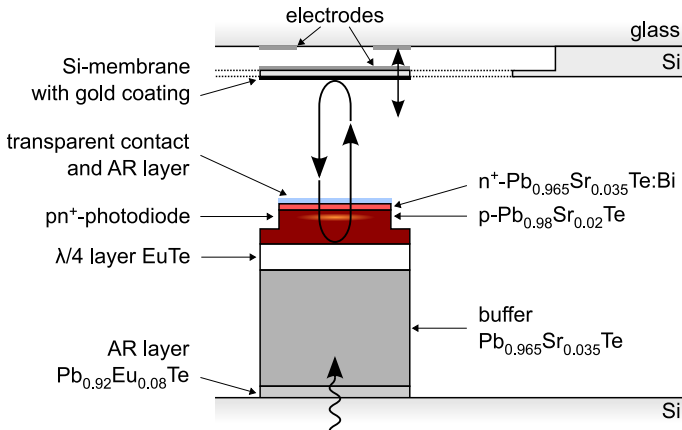


Figure 2.24: Schematics of a RCED using a PbSrTe heterojunction as photodiode. The Sr content in the absorber layer shifts the bandgap to shorter wavelengths.

with low R_1 and a large aperture setting of the measurement FTIR, see section 2.5.

The sensitive wavelength range of the RCED can be shifted to even shorter wavelengths, by either adding more Sr to the absorber layer, or by increasing the operation temperature. When operating at 240 K, the sensitive range spans from 3 μm to 3.5 μm .

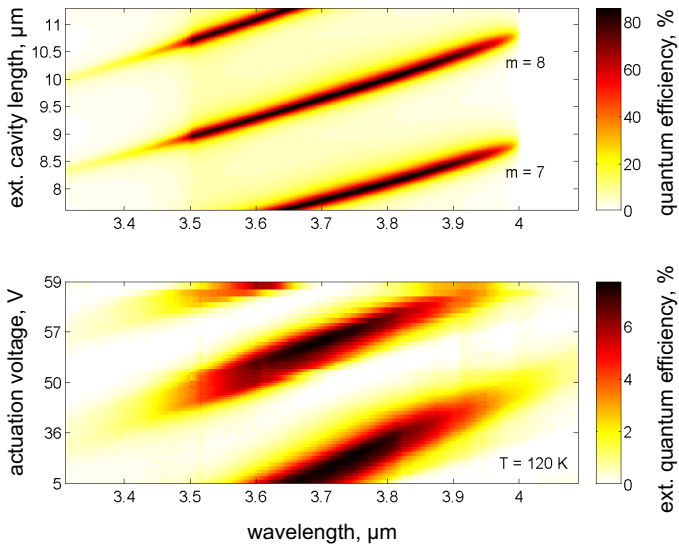


Figure 2.25: (top) Color-coded quantum efficiency of a Pb-SrTe RCED calculated for different cavity lengths, and (bottom) measured for different actuation voltages (BG corrected).

2.6.3 PbSnTe RCED for Longer Wavelengths

With increasing Sn content the cut-off wavelength of PbSnTe is shifted towards longer wavelengths. Figure 2.26 shows the schematics of a RCED using a $p\text{-Pb}_{1-y}\text{Sn}_y\text{Te}/n^+\text{-PbTe:Bi}$ heterojunction as photodiode. The buffer layer in this case is $\text{Pb}_{1-x}\text{Sn}_x\text{Te}$ as well, with a lower Sn concentration $x < y$. The lower mirror is a DBR with 1.5 pairs of EuTe/PbTe $\lambda/4$ layers. Since the absorber layer is only 50 nm thin, an additional PbTe contact layer is used to assure a sufficient low electric resistance.

Figure 2.27 shows the Color-coded quantum efficiency calculated for different cavity lengths, and the measured response curves for different actuation voltages (background corrected, 8 mm aperture). The device is sensitive from ~ 6.2 μm up to ~ 7.7 μm . Due to the width of this sensitivity range the signal is multi-mode, with mode orders 7 and 8 being detected. The calculation is performed for 100 K with Sn concentrations of $x = 6\%$ in the buffer and $y = 11.5\%$ in the absorber layer. The

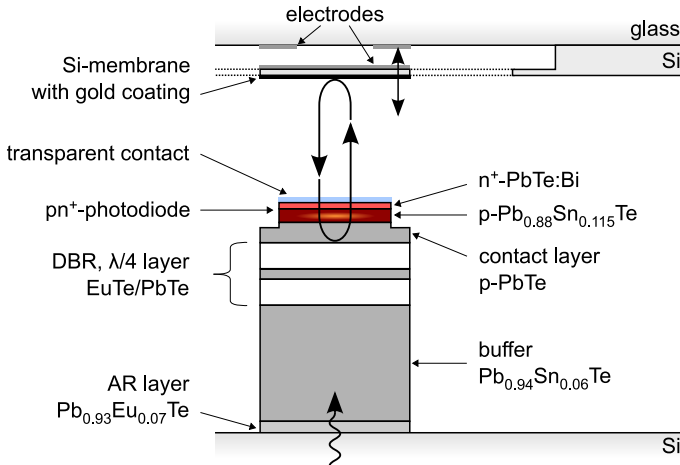


Figure 2.26: Schematics of a RCED using a PbSnTe heterojunction as photodiode. The Sn content in the absorber layer shifts the bandgap to longer wavelengths.

external cavity length is $15\ \mu\text{m}$ or more.

With increasing actuation voltage the resonances shift towards shorter wavelengths at first. At $80\ \text{V}$ the direction changes and the resonance wavelengths now shift towards longer wavelengths. Also the distance between the two resonances seems to decrease significantly with increasing cavity length. It is unclear what kind of movement of the mirror membrane causes this behavior. The shift of resonance wavelength is however completely repeatable, hence no mechanical deformation occurs. One possible explanation is some kind of tilt movement, where at least part of the mirror membrane initially moves towards the diode chip.

The FWHM of the resonance peak at $7.4\ \mu\text{m}$ is $\sim 210\ \text{nm}$, $\Delta\lambda/\lambda = 2.8\ \%$. This is partly due to the $8\ \text{mm}$ aperture setting of the measurement FTIR and the resulting large beam opening

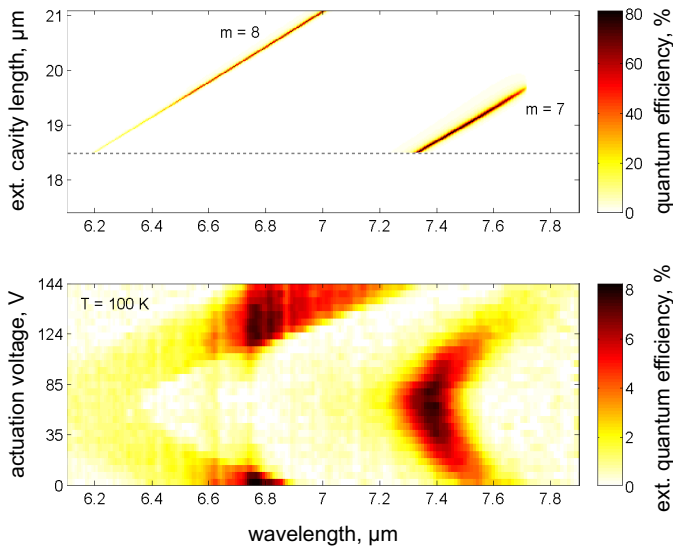


Figure 2.27: (top) Color-coded quantum efficiency of a Pb-SnTe RCED calculated for different cavity lengths, and (bottom) measured for different actuation voltages (BG corrected).

angle. Additionally, the mirror planes are most likely not very well aligned, as it can be expected for such an undefined mirror movement.

Devices with even longer wavelengths may be fabricated by increasing the Sn content in the absorber layer. Since the PbTe contact layer remains unchanged in this case, no significant penalty of the electronic properties of the device is expected.

Chapter 3

PbTe Quantum Dots

A major disadvantage of conventional QD detectors is their low quantum efficiency due to a very low absorption. The absorption can be improved to some extent by optimizing dot shape and size, and dot uniformity [27, 83]. However, for good absorption additionally a very high dot density is needed. This is typically not the case for self-assembled QD realized up to date, even for multiple stacked QD layers. In a resonant cavity enhanced setup however, the density may be lower. Photons entering the cavity are reflected many times between the mirrors, effectively increasing the total absorbance.

Figure 3.1 shows a QD sample after growth. The BaF_2 layer is water soluble and allows an epitaxial layer liftoff process. The CdTe buffer layer is several μm thick. It is the host matrix for the QD. The active PbTe layer is grown on top with a mean

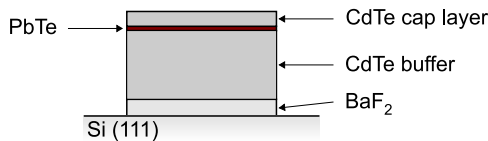


Figure 3.1: QD sample after growth. The PbTe layer is transformed to QD by phase separation during annealing.

thickness ranging from 2 nm to 50 nm. The final CdTe cap-layer is 10 nm to 1 μm thick. After growth, the PbTe layer is converted to QD by annealing. This is not done within the MBE chamber, but either on a hotplate at air or in a vacuum oven. The dot formation is caused by phase separation due to the different crystal structure of PbTe and CdTe [59]. This is completely different from the formation of other, e.g. using III-VI materials, self-assembled QD. There the QD are typically obtained with Stranski-Krastanow growth mode. Due to the different formation process no wetting layer remains.

3.1 Transition Energies

The transition energies of thin layers and QD are shifted due to strain as well as due to quantization effects. The formulas used for the here presented approximation can be found in any quantum mechanics text book. A more detailed description of the calculation is given elsewhere [84].

Strain is caused by the mismatch of lattice constants and the different thermal expansion coefficients of the CdTe host and the PbTe precipitate. It can be assumed that the strain is induced exclusively into the PbTe. The strain, calculated with the temperature dependency of the lattice constants l_i , is given by

$$\epsilon_0 = \frac{l_{CdTe}}{l_{PbTe}} - 1 \quad (3.1)$$

and the deformation potential D_{ISO} yield the bandgap shift

$$\Delta E_{g, strain} = \epsilon_0 D_{ISO} . \quad (3.2)$$

The deformation potential is temperature dependent [85].

The energies states of the QD can be numerically estimated using the Schrödinger equation for a square box with finite potential. The calculation is performed with the well known boundary conditions of the wave function. The even/odd solu-

tions for the wave vectors in the conduction band $k_{C,i}^2$ are

$$\frac{\hbar^2 k_{C,i}^2}{2m_{PbTe,i}^*} \left(1 + \frac{m_{CdTe}^*}{m_{PbTe,i}^*} \left\{ \frac{\tan(k_{C,i} \frac{d}{2})^2}{\cot(k_{C,i} \frac{d}{2})^2} \right\} \right) - \Delta E_C = 0 \quad (3.3)$$

where

i	directions \hat{x} , \hat{y} , \hat{z} ,
$m_{PbTe,i}^*$	effective mass of electrons in PbTe ,
m_{CdTe}^*	effective mass of electrons in CdTe,
d	size of the QD,
ΔE_C	conduction band offset.

The nomenclature is given in figure 3.2. The calculation of the wave vectors in the valence band is alike, with the effective masses for holes and the valence band offset ΔE_V . The effective masses of both carriers depend on type and direction, as listed in table 3.1 [86]. They also depend on temperature

$$m_i^*(T) = m_i^*(T_0) \frac{E_g(T)}{E_g(T_0)} .$$

As an approximation the total transition energy for a QD is the sum over all directions for electrons and holes

$$\Delta E_{g,quant} = \sum_{x,y,z} \sum_{e,h} E_{i,j} \quad (3.4)$$

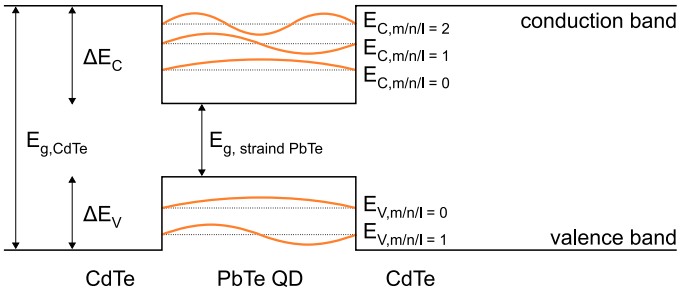


Figure 3.2: Sketched band structure of a PbTe QD. The quantum numbers m, n, l correspond to the \hat{x} , \hat{y} , \hat{z} directions.

valley	m_x^*	m_y^*	m_z^*
longitudinal	m_t^*	m_t^*	m_l^*
oblique	m_t^*	$\frac{9m_i^*m_l^*}{m_t^*+8m_l^*}$	$\frac{9m_i^*m_l^*}{8m_t^*+m_l^*}$

Table 3.1: *PbTe* effective masses [86].

with the energy levels

$$E_{i,j} = \frac{\hbar^2 k_{C,i}^2}{2m_{PbTe,i}^*}. \quad (3.5)$$

This does not take the coupling of states for the different directions into account. A proper calculation could be done using a sphere shaped potential. However, the error caused by the very uncertain material properties D_{ISO} and m_i^* of IV–VI materials is much greater than the variance caused by the approximation. The estimation of QD size is used, in conjunction with experimental data from SEM and STEM investigations, as basis for the interpretation of photoluminescence spectra.

3.2 Formation of PbTe QD

The PL spectra recorded at 110 K for different annealing temperatures are shown in figure 3.3. The used samples are from one wafer, with an originally 10 nm mean thickness of the PbTe layer and an 1 μm thick cap layer. Annealing duration for each sample is 1 h. Two distinct emission peaks A and B are visible, at ~ 0.31 eV and at ~ 0.43 eV respectively. The peak A at lower energies does not shift during annealing. It is also faintly visible in unannealed samples. The peak B at higher energies appears after the first annealing step. It shifts towards higher energies with higher annealing temperatures before it vanishes for annealing above 340°C.

All processed samples show either both peaks A and B, or they show either peak A or peak B. For the same measurement temperatures the emission energies of each peak are effectively

equal for all samples similarly annealed. The mean thicknesses of the deposited PbTe layer and the thickness of the cap layer determine the emission spectra. Samples with a PbTe layer thinner 50 nm and a cap layer greater 50 nm show both peaks A and B, with peak B vanishing with increasing annealing temperature (figure 3.3). For samples with a PbTe layer greater 50 nm only the emission peak A appears regardless of cap layer and annealing conditions. Samples with PbTe and CdTe cap layer smaller 10 nm emit only at the high energy peak B.

A sample with an originally 8 nm thick PbTe layer and a 1 μm CdTe cap layer was annealed at 360°C for 4 h. Emission occurs at peak A only, at ~ 0.31 eV for 100 K, see figure 3.4. With higher measurement temperatures the emission is blue-shifted. Figure 3.5 shows the cross-section STEM high angle annular dark field image of this sample. PbTe precipitates with a height of greater 30 nm and a width of several hundred nm are visible. As depicted in the insets, their trapezoidal shape results from the intersection of the (100), (010), and (001) facets with the (1-11) viewing plane. Due to the threefold symmetry of the (111)

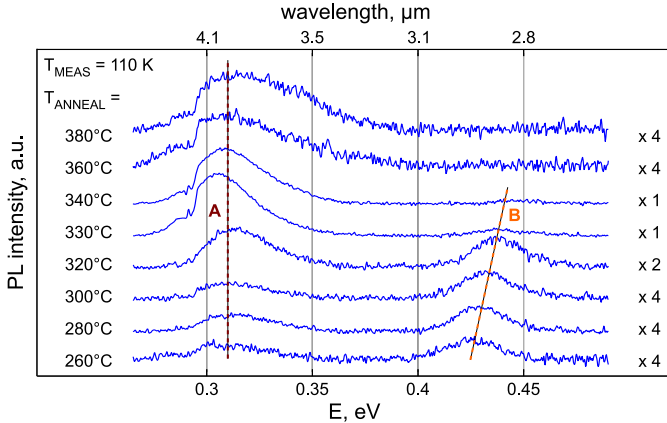


Figure 3.3: *PL spectra measured at 110 K of samples annealed at different temperatures. As the dashed lines indicate, the peak B at ~ 0.43 eV is blue-shifted with higher annealing temperatures, while the lower energy peak A does not shift.*

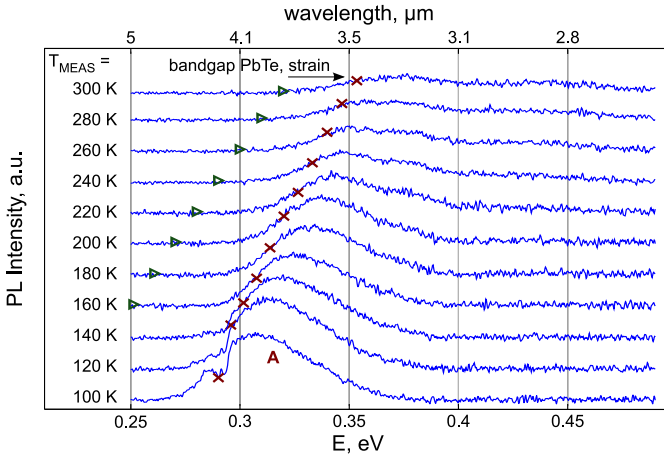


Figure 3.4: PL spectra of a sample with originally 8 nm PbTe embedded 1 μm deep within the CdTe, annealed at 360°C. The markers represent the PbTe bandgap (unstrained \triangleright , strained \times).

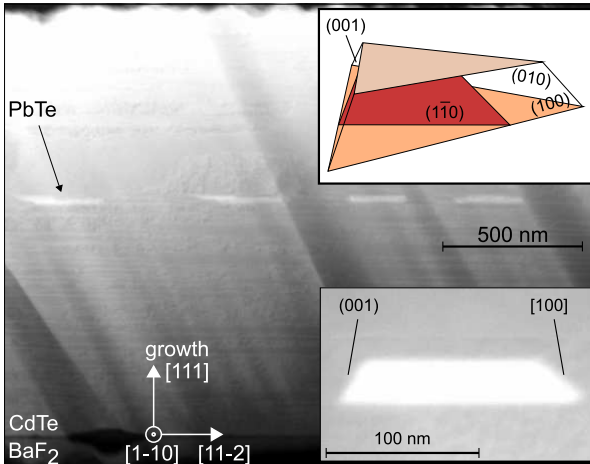


Figure 3.5: STEM image of an annealed sample with originally 8 nm PbTe deeply embedded (1 μm) within the CdTe. (insets) The PbTe precipitates are in the shape of truncated pyramids.

plane, it can be concluded that the precipitates are truncated pyramids. Due to their large size no quantization effects are apparent. The shifted bandgap of emission peak A relates to the strain induced by the host matrix.

A sample with an originally 7 nm thick PbTe layer and a 10 nm cap layer annealed for 4 h at 320°C emits only at peak B at ~ 0.45 eV, as shown in figure 3.6. With higher measurement temperatures the emission is slightly red-shifted. SEM and STEM images are shown in figure 3.7. The SEM image was taken with a tilted view of 55° to reduce the influence of surface roughness on the image contrast. Brighter spots corresponding to higher atomic mass indicate PbTe QD beneath the cap layer. Their counted density is $\sim 2 \cdot 10^{10} \text{ cm}^{-2}$, however the real value may be greater due to the limited penetration depth of the SEM. For an initial PbTe layer thickness of 7 nm this yields an average cubic dot size smaller 32 nm. In the cross-section STEM image (inset) QD with a height of ~ 10 nm and a width of 10 nm to 20 nm are visible. It is however unknown whether and to what extend parts of the QD may have been removed during the preparation process. EDX measurements of a QD and the surrounding host material confirm the additional Pb content in the QD.

The markers in figure 3.6 represent the emission energies for the longitudinal and oblique (100) to (100) interband transitions of a QD with a size of 20 nm. They are calculated using the approximation presented in section 3.1. Since the parities of the Bloch functions in the valence and the conduction band of PbTe are different, transitions without parity change are favored [42]. Additionally the incoming pump beam is quasi perpendicular to the QD plane. Light is a transversal wave and there is no excitation in the \hat{z} (1) direction possible. Expected transitions are then of the type nm0 to nm0. The calculated values reproduce the temperature-dependence of the emission peak very well, owing to the change of effective masses proportional to $E_g(T)$.

From the PL measurements in conjunction with the SEM and STEM images a conclusion on the formation of the QD is possible. The deposition of PbTe does not produce individual

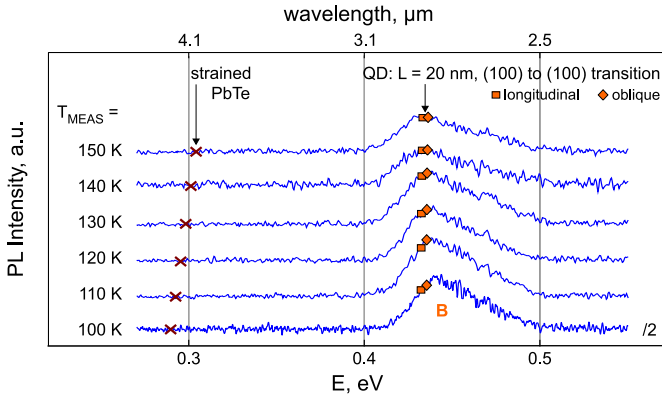


Figure 3.6: PL spectra of a sample with originally 7 nm PbTe and a 10 nm thick cap layer, annealed at 320°C. The markers represent the longitudinal and oblique (100) to (100) interband transitions of QD with a size of 20 nm.

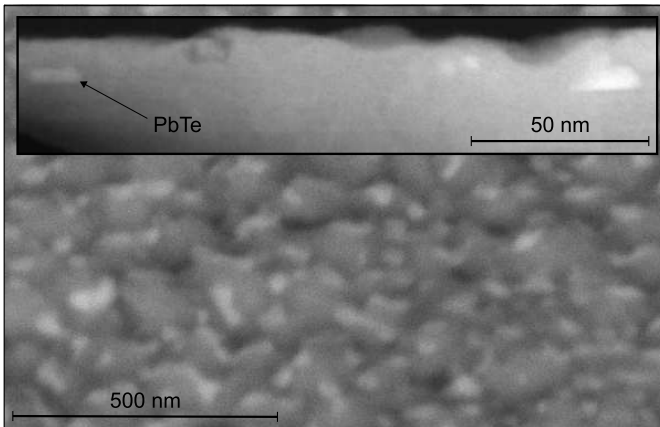


Figure 3.7: Back scatter SEM image taken 55° inclined of an annealed sample with originally 7 nm PbTe and a 10 nm thick cap layer. QD density is $\sim 2 \cdot 10^{10} \text{ cm}^{-2}$, yielding a average dot size smaller 32 nm. (inset) In the cross-section STEM image at least two PbTe QD are identifiable.

QD, but a connected PbTe film. Its original thickness may be nonuniform due to surface roughness of the CdTe buffer. For any sample with a thin PbTe layer deeply embedded in the CdTe host, annealing at low temperatures below 300°C leads to the formation of QD as well as larger PbTe precipitates. Additional annealing at increasing temperatures leads to diffusion of material from the smaller dots towards the larger precipitates. The diffusion yields a reduced size of the dots, thus a stronger quantization. This is seen as a blue-shift of the emission peak B in figure 3.3. For annealing temperatures above 340°C all the remaining PbTe aggregates in the large precipitates, and the QD emission peak B disappears. For a thin cap layer only small QD and no large precipitates are formed during annealing.

This behavior for (111) orientation is at variance to results obtained with other orientations or host materials. For example size-controllable PbTe QD in CdTe have been reported on GaAs(100) substrates [36]. In conjunction with here obtained results, this indicates a very anisotropic diffusion of the PbTe within the CdTe host, with much higher values in the (111) plane. Diffusion is however hindered for thin cap layers. Since the thickness of the cap layer is equal or less than the surface roughness of the CdTe host, this is possibly due to the final interface to air acting as a diffusion boundary during annealing. A resembling effect has been observed for PbTe host layers, where self-assembled PbSe QD with originally pyramidal shape were truncated during overgrowth [31]. According to that study, alloying the host with Eu hinders diffusion. In a different work, ultra thin EuTe or SrTe intermediate layers have been employed as stabilizing barriers [32]. Nevertheless, due to this high diffusion, the sizes of PbTe QD in a CdTe(111) host are not as controllable as required for the use in an infrared detector.

Chapter 4

Conclusion

Tunable resonant cavity enhanced detectors (RCED) were fabricated. They are sensitive in the MIR wavelength region and offer unique properties. Single-mode detection of a narrow resonance peak, which is tunable over a broad wavelength range, has been demonstrated.

PbTe and alloys thereof were used, grown epitaxially on silicon substrate. Different detection wavelength ranges were achieved by alloying of the absorber layer, as well as by thermal tuning. Devices sensitive around $\sim 3.5 \mu\text{m}$, $\sim 5 \mu\text{m}$, and $\sim 7.5 \mu\text{m}$ were realized. With higher alloying even shorter and longer wavelength are achievable. The devices operate at temperatures up to $> 240 \text{ K}$. Above 200 K they can be cooled thermo-electrically. For such high operation temperatures, the sensitivity of the thin photodiodes is higher than the diffusion limit for band-to-band recombination of a comparable conventional bulk detector layer. Further sensitivity enhancements are still possible, e.g. by improving the crystal quality of the active layers. Depending on device and measurement design, the single detection peak is very narrow, with an measured FWHM of 35 nm . This is limited mainly by the cone angle of the measurement setup and by the parallelism of the mirror planes. By collimating the incoming beam, e.g. with a plano-convex high refractive index material, and increasing the cavity finesse with

an improved process, this value may still be reduced significantly.

The detection peak is tunable over an at least $0.5\ \mu\text{m}$ wide wavelength range. By reducing the cavity length this range can be extended to $> 1\ \mu\text{m}$ width. The tunability was achieved with vertically movable micro-electro-mechanical-system (MEMS) micro-mirrors. When fabricated as 2D arrays, large adaptive focal plane arrays may be realized, where the detection wavelength of each pixel or groups of pixels may be tuned individually during operation.

The growth of self assembled PbTe QD in a CdTe(111) host matrix on Si(111) has been studied. Dot formation during annealing depends heavily on the thickness of the overgrowth layer. A very thin cap layer with a thickness in the order of the CdTe surface roughness acted as a diffusion barrier. Such samples formed QD smaller than 20 nm. The formation of PbTe QD on Si(111) proved to be quite different from results using (100)-orientated GaAs substrates. This indicates a very anisotropic diffusion. As a further improvement of the RCED concept, a quantum dot infrared photodetector may be integrated within the resonant cavity. This should lead to even more enhanced detector characteristics such as signal-to-noise ratio and peak width.

Appendix – MIR Absorption lines

Figure 4.1 shows the MIR absorption lines of relevant gases. Also shown is the absorption of water and its atmospheric transparency windows. All datasets are taken from the HiTran 2004 database [87].

The upper graph shows the main combustion gases CO_2 , CO , NO_2 , NO and SO_2 . Also shown is O_3 , a toxic byproduct which is created from NO_2 and O_2 in combination with UV radiation. The lower graph shows the hydrocarbons CH_4 (methane), C_2H_6 (ethane), C_2H_2 (ethyne, acetylene), and C_2H_4 (ethene, ethylene). With the ban of chlorofluorocarbons (CFC) N_2O (laughing gas) became the dominant substance damaging the ozone layer. It is created in soil due to overfertilization and by the 3-way catalytic converter used in modern combustion engines. H_2O_2 is a base substance for the explosive acetone peroxide (TATP).

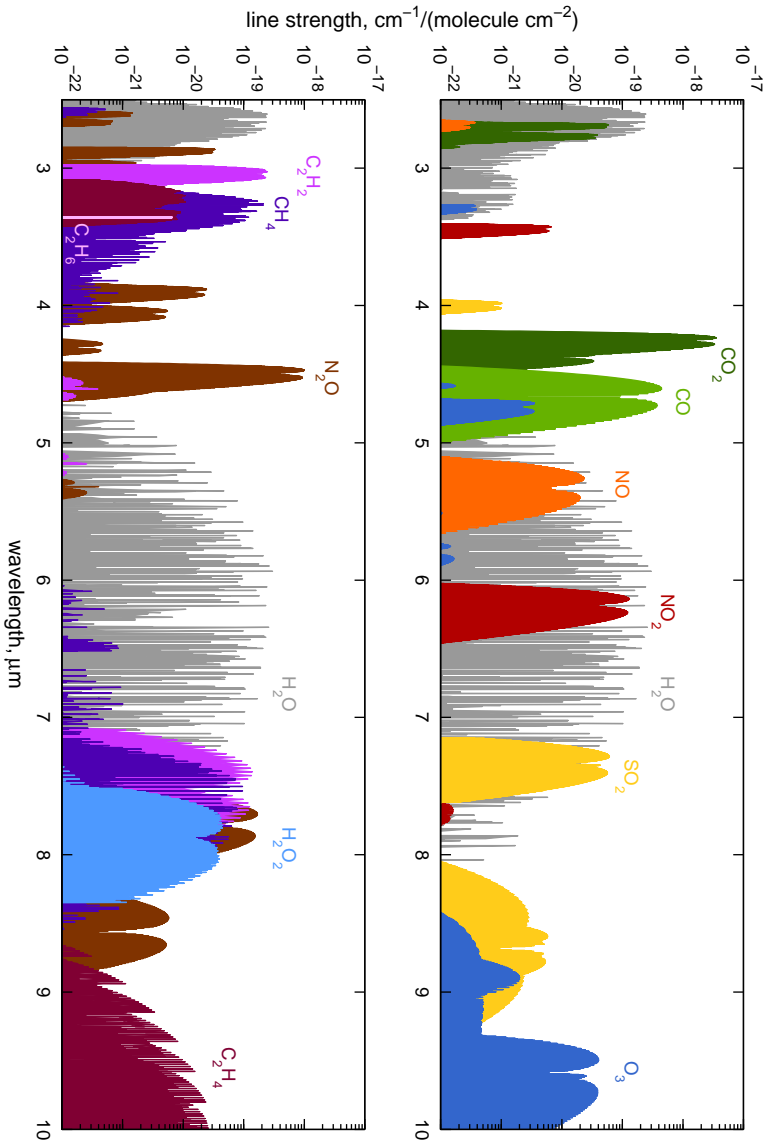


Figure 4.1: MIR absorption lines of important gases [87].

Bibliography

- [1] S. Pal, K. B. Ozanyan, H. McCann, *A spectroscopic study for detection of carbon-monoxide using mid-infrared techniques for single-pass measurement*, **J. Phys.: Conf. Ser.** **85**, 012020, 2007
- [2] U. Willer, M. Saraji, A. Khorsandi, P Geiser, W. Schade, *Near- and mid-infrared laser monitoring of industrial processes, environment and security applications*, **Optics and Lasers in Engineering** **44**, 7, pp. 699-710, 2006
- [3] P. Norton, *Third-generation sensors for night vision*, **Opto-Electronics Review** **14**, 2006
- [4] C. A. Balaras, A. A. Argiriou, *Infrared thermography for building diagnostics*, **Energy and Buildings** **34** (2), pp. 171-183, 2002
- [5] Deltron AG, *www.deltron.ch*
- [6] M. S. Ünlü, S. Strite, *Resonant cavity enhanced photonic devices*, **Journal of Applied Physics** **78**, 1995
- [7] L. P. Schuler, J. S. Milne, J. M. Dell, L. Faraone, *MEMS-based microspectrometer technologies for NIR and MIR wavelengths*, **J. Phys. D: Appl. Phys.** **42**, 133001, 2009
- [8] H. Zogg, *Lead Chalcogenides: Physics and Applications*, in *Optoelectronic Properties of Semiconductors and Superlattices*, D. Khokhlov ed., 18, Taylor & Francis, 2003

- [9] M. Arnold, D. Zimin, H. Zogg, *Resonant-cavity-enhanced photodetectors for the mid-infrared*, **Appl. Phys. Lett.** **87**, 14, pp. 141103, 2005
- [10] M. Arnold, D. Zimin, K. Alchalabi, H. Zogg, *Lead salt mid-IR photodetectors with narrow linewidth*, **Journal of Crystal Growth** **278**, pp. 739-742, 2005
- [11] M. Arnold, *Mid-Infrared Semiconductor Devices with Vertical Cavities*, ETH Zürich, DISS #17507, 2007
- [12] H. Zogg, K. Alchalabi, D. Zimin, K. Kellermann, *Two-dimensional monolithic lead chalcogenide infrared sensor arrays on silicon read-out chips and noise mechanisms*, **IEEE Trans. Electron Devices** **50**, 1, pp. 209- 214, 2003
- [13] J. G. A. Wehner, C. A. Musca, R. H. Sewell, J. M. Dell, L. Faraone, *Mercury cadmium telluride resonant-cavity-enhanced photoconductive infrared detectors*, **Appl. Phys. Lett.** **87**, 211104, 2005
- [14] A. Green, D. Gevaux, C. Roberts, P. Stavrinou, C. Phillip, $\lambda \approx 3 \mu\text{m}$ *InAs resonant-cavity-enhanced photodetector*, **Semiconductor Science and Technology** **18**, pp. 964-967, 2003
- [15] K. Xie, J.H. Zhao, Y. Shi, H. Lee, G. Olsen, *Resonant cavity enhanced GaInAsSb-AlAsSb photodetector grown by MBE for mid-IR applications*, **Photonics Technology Letters** **8**, 5, pp. 667-669, 1996
- [16] K. Liu, Y. Huang, X. Ren, *Theory and Experiments of a Three-Cavity Wavelength-Selective Photodetector*, **Applied Optics** **39**, 24, pp. 4263-4269, 2000
- [17] M.S. Wu, E.C. Vail, G.S. Li, W. Yuen, C.J. Chang-Hasnain, *Widely and Continuously Tunable Micromachined Resonant Cavity Detector with Wavelength Tracking*, **Photonics Technology Letters**, **IEEE** **8**, 1996
- [18] R. F. Wolffenbuttel, *MEMS-based optical mini-and microspectrometers for the visible and infrared spectral*

- range*, **Journal of Micromechanics and Microengineering** **15**, 2005
- [19] C. A. Musca, J. Antoszewski, K. J. Winchester, A. J. Keating, T. Nguyen, K. K. M. B. D. Silva, J. M. Dell, L. Faraone, P. Mitra, J. D. Beck, M. R. Skokan, J. E. Robinson, *Monolithic integration of an infrared photon detector with a MEMS-based tunable filter*, **Electron Device Letters** **26**, 12, pp. 888-890, 2005
- [20] N. Neumann, M. Ebermann, K. Hiller, S. Kurth, *Tunable infrared detector with integrated micromachined Fabry-Perot filter*, **Proc. MOEMS and Miniaturized Systems VI Proc. SPIE**, Vol. **6466**, 64660, 2007
- [21] Laser Components Group, www.lasercomponents.com
- [22] S. P. Tobin, M. H. Weiler, M. A. Hutchins, T. Parodos, P. W. Norton, *Advances in composition control for 16 μm LPE P-on-n HgCdTe heterojunction photodiodes for remote sensing applications at 60K*, **J. Electr. Mat.** **28**, 6, pp. 596-602, 1999
- [23] S. Tsao, H. Lim, W. Zhang, and M. Razeghi, *High operating temperature 320x256 middle-wavelength infrared focal plane array imaging based on an InAs/InGaAs/InAlAs/InP quantum dot infrared photodetector*, **Appl. Phys. Lett.** **90**, 201109, 2007
- [24] S. Krishna, D. Forman, S. Annamalai, P. Dowd, P. Varangis, T. Tumolillo, Jr, A. Gray, J. Zilko, K. Sun, M. Liu, J. Campbell, D. Carothers, *Demonstration of a 320x256 two-color focal plane array using InAs/InGaAs quantum dots in well detectors*, **Appl. Phys. Lett.** **86**, 193501, 2005
- [25] D. Hofstetter, M. Graf, T. Aellen, J. Faist, L. Hvozdar, S. Blaser, *23 GHz operation of a room temperature photovoltaic quantum cascade detector at 5.35 μm* , **Appl. Phys. Lett.** **89**, 061119, 2006
- [26] D. Hofstetter, F. R. Giorgetta, E. Baumann, Q. Yang, C. Manz, K. Köhler, *Midinfrared quantum cascade detector*

- with a spectrally broad response*, **Appl. Phys. Lett.** **93**, 221106, 2008
- [27] J. Phillips, *Evaluation of the fundamental properties of quantum dot infrared detectors*, **J. Appl. Phys.** **91**, 4590, 2002
- [28] R. S. Attaluri, J. Shao, K. T. Posani, S. J. Lee, J. S. Brown, A. Stintz, S. Krishna, *Resonant cavity enhanced InAs/In_{0.15}Ga_{0.85}As dots-in-a-well quantum dot infrared photodetector*, **J. Vac. Sci. & Technol. B** **25**, 4, pp. 1186-1190, 2007
- [29] M. Böberl, T. Fromherz, T. Schwarzl, G. Springholz, W. Heis, *IV-VI resonant-cavity enhanced photodetectors for the mid-infrared*, **Semiconductor Science and Technology** **19**, 2004
- [30] K. Alchalabi, D. Zimin, G. Kostorz, H. Zogg, *Self-Assembled Semiconductor Quantum Dots with Nearly Uniform Sizes*, **Phys. Rev. Lett** **90**, pp. 026104, 2003
- [31] L. Abtin, G. Springholz, V. Holy, *Surface Exchange and Shape Transitions of PbSe Quantum Dots during Overgrowth*, **Phys. Rev. Lett.** **97**, 266103, 2006
- [32] L. Abtin, G. Springholz, *Stabilization of PbSe quantum dots by ultrathin EuTe and SrTe barrier layers*, **Appl. Phys. Lett.** **93**, 163102, 2008
- [33] M. Simma, T. Fromherz, A. Raab, G. Springholz, G. Bauer, *Lateral photocurrent spectroscopy on self-assembled PbSe quantum dots*, **Appl. Phys. Lett.** **88**, 201105, 2006
- [34] K. Koike, T. Itakura, T. Hotei, M. Yano, *Molecular beam epitaxial growth and photoluminescence characterization of self-organized Pb_{1-x}Sn_xTe quantum dots embedded in a single-crystalline CdTe host matrix*, **Appl. Phys. Lett.** **91**, 181911, 2007
- [35] K. Koike, H. Harada, T. Itakura, M. Yano, W. Heiss, H. Groiss, E. Kaufmann, G. Hesser, F. Schäffler, *Photoluminescence characterization of PbTe/CdTe quantum*

- dots grown by lattice-type mismatched epitaxy*, **J. Cryst. Growth** **301**, pp. 722, 2007
- [36] H. Groiss, E. Kaufmann, G. Springholz, T. Schwarzl, G. Hesser, F. Schaffler, W. Heiss, K. Koike, T. Itakura, T. Hotei, M. Yano, T. Wojtowicz, *Size control and midinfrared emission of epitaxial PbTe/CdTe quantum dot precipitates grown by molecular beam epitaxy*, **Appl. Phys. Lett.** **91** **91**, 222106, 2007
- [37] E. Kaufmann, T. Schwarzl, H. Groiss, G. Hesser, F. Schaffler, L. Palmetshofer, G. Springholz, W. Heiss, *PbTe and SnTe quantum dot precipitates in a CdTe matrix fabricated by ion implantation*, **J. Appl. Phys.** **106**, 4, pp. 043105, 2009
- [38] P. C. Findlay, C. R. Pidgeon, R. Kotitschke, A. Hollingworth, B. N. Murdin, C. J. G. M. Langerak, A. F. G. van der Meer, C. M. Ciesla, J. Oswald, A. Homer, G. Springholz, G. Bauer, *Auger recombination dynamics of lead salts under picosecond free-electron-laser excitation*, **Phys. Rev. B** **58**, 19, pp. 12908-12915, 1998
- [39] J. Piotrowski, *Uncooled operation of IR photodetectors*, **Opto-Electronics Review** **12**, 1, pp. 111-122, 2004
- [40] *Lead telluride (PbTe) crystal structure, lattice parameters, thermal expansion*, in *Landolt-Börnstein, Condensed Matter*, III/41C, Springer, 1998
- [41] J. N. Zemel, J. D. Jensen, R. B. Schoolar, *Electrical and Optical Properties of Epitaxial Films of PbS, PbSe, PbTe, and SnTe*, **Phys. Rev.** **140**, 1A, pp. A330-A342, 1965
- [42] G. Martinez, M. Schlüter, M. L. Cohen, *Electronic structure of PbSe and PbTe. I. Band structures, densities of states, and effective masses*, **Phys. Rev. B** **11**, pp. 651-659, 1975
- [43] S. Yuan, H. Krenn, G. Springholz, G. Bauer, *Dispersion of absorption and refractive index of PbTe and Pb_{1-x}Eu_xTe (x<0.05) below and above the fundamental gap*, **Phys. Rev. B** **47**, 12, pp. 7213 - 7226, 1993

- [44] A. Ishida, S. Matsuura, M. Mizuno, Y. Sase, H. Fujiyasu, *Properties of Pb_{1-x}Eu_xTe films prepared by hot-wall epitaxy*, **J. Appl. Phys.** **63**, 9, pp. 4572, 1988
- [45] D. L. Partin, C. M. Thrush, B. M. Clemens, *Lead strontium telluride and lead barium telluride grown by molecular-beam epitaxy*, **J. Vac. Sci. Technol. B** **5**, 3, pp. 686-689, 1987
- [46] R. N. Tauber, I. B. Cadoff, *Thermal and Optical Energy Gaps in Pb_{0.93}Sn_{0.07}Te and Pb_{0.85}Sn_{0.15}Te*, **J. Appl. Phys.** **38**, 3714, 1967
- [47] F. Sizov, M. Apatskaya, J. Gumenjuk-Sichevskaya, V. Tetyorkin, Y. Troyan, *Electronic properties of PbTe-PbSnTe Multiple quantum wells*, **Semicond. Sci. Technol.** **5**, pp. 928-932, 1990
- [48] *EuTe: crystal structure, physical properties*, in *Landolt-Börnstein, Condensed Matter*, III/41D, Springer, 2000
- [49] P. Wachter, *Refractive index and dispersion of the Europium-Chalcogenides*, **Phys. kondens. Materie** **8**, 1, pp. 80-86, 1968
- [50] *Cadmium telluride (CdTe) lattice parameter, thermal expansion*, in *Landolt-Börnstein, Condensed Matter*, III/41B, Springer, 1999
- [51] *Cadmium telluride (CdTe) optical properties, refractive index, dielectric constants, two-photon absorption*, in *Landolt-Börnstein, Condensed Matter*, III/41B, Springer, 1999
- [52] G. Fonthal, L. Tirado-Mejía, J. I. Marín-Hurtado, H. Ariza-Calderón, J. G. Mendoza-Alvarez, *Temperature dependence of the band gap energy of crystalline CdTe*, **Journal of Physics and Chemistry of Solids** **91**, 4, pp. 579-583, 2000
- [53] *Silicon (Si), refractive index*, in *Landolt-Börnstein, Condensed Matter*, III/41A1b, Springer, 2002

- [54] *Silicon (Si) thermal expansion*, in *Landolt-Börnstein, Condensed Matter*, III/41A1a, Springer, 2001
- [55] *Silicon (Si), indirect energy gap*, in *Landolt-Börnstein, Condensed Matter*, III/41A1b, Springer, 2002
- [56] *Simple fluorides and their solid solutions*, in *Landolt-Börnstein, Condensed Matter*, III/7A, Springer, 1993
- [57] W. L. Wolfe, G. J. Zissis, , in *The Infrared Handbook*, 3rd edition, Environmental Research Institute of Michigan, 1989
- [58] D. R. Lide, , in *CRC Handbook of Chemistry and Physics*, 74th edition, CRC PRes, 1993-94
- [59] W. Heiss, H. Groiss, E. Kaufmann, G. Hesser, M. Böberl, G. Springholz, F. Schäffler, K. Koike, H. Harada, M. Yano, *Centrosymmetric PbTe/CdTe quantum dots coherently embedded by epitaxial precipitation*, **Appl. Phys. Lett.** **88**, 192109, 2006
- [60] J. Si, S. Jin, H. Zhang, P. Zhu, D. Qiu, H. Wu, *Experimental determination of valence band offset at PbTe/CdTe(111) heterojunction interface by x-ray photoelectron spectroscopy*, **Appl. Phys. Lett.** **93**, 202101, 2008
- [61] D. L. Partin, C. M. Thrush, S. J. Simko, S. W. Gaarenstroom, *Bismuth- and thallium-doped lead telluride grown by molecular-beam epitaxy*, **J. Appl. Phys.** **66**, 12, pp. 6115-6120, 1989
- [62] H. Zogg, S. Blunier, A. Fach, C. Maissen, P. Müller, S. Teodoropol and V. Meyer, G. Kostorz, A. Dommann, T. Richmond, *Thermal-mismatch-strain relaxation in epitaxial CaF₂, BaF₂/CaF₂, and PbSe/BaF₂/CaF₂ layers on Si(111) after many temperature cycles*, **Phys. Rev. B** **50**, 15, pp. 10801-10810, 1994
- [63] H. Zogg, S. Blunier, *Molecular beam epitaxial growth of high structural perfection CdTe on Si using a (Ca,Ba)F₂ buffer layer*, **Appl. Phys. Lett.** **49**, pp. 1531-1534, 1986

- [64] H. Zogg, *Strain relief in epitaxial fluoride buffer layers for semiconductor heteroepitaxy*, **Appl. Phys. Lett.** **49**, 15, pp. 933-935, 1986
- [65] J. M. Bennett, E. J. Ashley, *Infrared Reflectance and Emittance of Silver and Gold Evaporated in Ultrahigh Vacuum*, **Applied Optics** **4**, 2, pp. 221-224, 1965
- [66] M. A. Ordal, L. L. Long, R. J. Bell, S. E. Bell, R. R. Bell, R. W. Alexander, C. A. Ward, *Optical properties of the metals Al, Co, Cu, Au, Fe, Pb, Ni, Pd, Pt, Ag, Ti, and W in the infrared and far infrared*, **Applied Optics** **22**, 7, pp. 1099-1120, 1983
- [67] H. A. Macleod, *Thin-Film Optical Filters*, 3. Edition, CRC Press, 2001
- [68] W. Heiss, T. Schwarzl, J. Roither, G. Springholz, M. Aigle, H. Pascher, K. Biermann, K. Reimann, *Epitaxial Bragg mirrors for the mid-infrared and their applications*, **Progress in Quantum Electronics** **25**, 5-6, pp. 193-228, 2001
- [69] L. J. van der Pauw, *A method of measuring specific resistivity and Hall effect of discs of arbitrary shape*, **Philips Res. Repts** **13**, 1, 1958
- [70] H. H. Wieder, *Electrical and galvanomagnetic measurements on thin films and epilayers*, **Thin Solid Films** **31**, 1-2, pp. 123-138, 1976
- [71] A. Rogalski, K. Adamiec, J. Rutkowski, , in *Narrow Gap Semiconductor Photodiodes*, SPIE, Bellingham, WA, 2000
- [72] J. John, H. Zogg, *Infrared p-n-junction diodes in epitaxial narrow gap PbTe layers on Si substrates*, **J. Appl. Phys.** **85**, 6, pp. 3364-3367, 1999
- [73] EMEZ - Electron Microscopy ETH Zurich, www.emez.ethz.ch
- [74] Center of Mechanics, ETH Zurich, www.zfm.ethz.ch

- [75] A. Rogalski, M. Razeghi, *Narrow-gap semiconductor photodiodes*, **Proc. SPIE** **3287**, pp. 2-13, 1998
- [76] D. Zimin, K. Alchalabi, H. Zogg, *Heteroepitaxial PbTe-on-Si pn-junction IR-sensors: correlations between material and device properties*, **Physica E** **13**, 2-4, pp. 1220-1223, 2002
- [77] A. Rogalski, R. Ciupa, H. Zogg, *Computer modeling of carrier transport in binary lead salt photodiodes*, **Proc. SPIE** **2373**, pp. 172-181, 1995
- [78] Chih-Tang Sah, R.N. Noyce, W. Shockley, *Carrier Generation and Recombination in P-N Junctions and P-N Junction Characteristics*, **Proc. of the IRE** **45**, 7, pp. 1228-1243, 1957
- [79] N. Quack, *Micromirrors for Integrated Tunable Mid-Infrared Detectors and Emitters*, ETH Zurich, DISS #18702, 2009
- [80] P. D. Atherton, N. K. Reay, J. Ring, T. R. Hicks, *Tunable Fabry-Perot filters*, **Optical Engineering** **20**, pp. 806-814, 1981
- [81] C. Roychoudhuri, M. Hercher, *Stable multipass Fabry-Perot interferometer: design and analysis*, **Applied Optics** **16**, 9, pp. 2514-2520, 1977
- [82] D. Eger, A. Zemel, S. Rotter, N. Tamari, M. Oron, A. Zussman, *Junction migration in PbTe-PbSnTe heterostructures*, **J. Appl. Phys.** **52**, 1, pp. 490-495, 1981
- [83] W. Zhang, H. Lim, M. Taguchi, S. Tsao, B. Movaghar, M. Razeghi, *High-detectivity InAs quantum-dot infrared photodetectors grown on InP by metal-organic chemical-vapor deposition*, **Appl. Phys. Lett.** **86**, 191103, 2005
- [84] A. Fognini, *Growth and Characterization of PbTe Quantum Dots in CdTe Host for Infrared Detectors*, Diploma thesis, ETH Zurich, 2008
- [85] I. I. Zasavitskii, E. A. de Andrada e Silva, E. Abramof, P. J. McCann, *Optical deformation potentials for PbSe and PbTe*, **Phys. Rev. B** **70**, 115302, 2004

- [86] Effects of band nonparabolicity on the gain and current density in EuSe-PbSe_{0.78}Te_{0.22}-EuSe IV-VI semiconductor quantum-well lasers, *M. F. Khodr, P. J. McCann, B. A. Mason*, **IEEE J. Quant. Elec.** **32**, 2, pp. 236-247, 1996
- [87] L.S. Rothman, et al, *HITRAN 2004*, **J. of Quantitative Spectroscopy and Radiative Transfer** **96**, pp. 139-204, 2005

Publications

Articles

27. M. Rahim, A. Khiar, F. Felder, M. Fill, D. Chappuis, M.W. Sigrist, H. Zogg, *5 μm Vertical External Cavity Surface Emitting Lasers (VECSEL) for Spectroscopic Applications*, TDLs 2009 Applied Physics B, 7th International Conference on Tunable Diode Laser Spectroscopy, submitted
26. H. Zogg, M. Rahim, F. Felder, M. Fill, A. Khiar, D. Chappuis, Lead chalcogenide mid-IR tunable lasers and narrow band detectors, **J. Modern Optics**, Proc. AITA 10, 10th International Workshop on Advanced Infrared Technology and Applications, in print
25. F. Felder, N. Quack, S. Blunier, M. Fill, M. Rahim, J. Dual, H. Zogg, *Narrow band tunable resonant cavity enhanced detectors for 3 - 10 μm wavelength*, **NIM A**, Proc. 11th European Symposium on Semiconductor Detectors, in print
24. H. Zogg, M. Rahim, F. Felder, M. Fill, D. Boye (invited), *Lead-chalcogenide sensors and lasers for the mid-infrared range*, Proc. 10th Takayanagi Kenjiro Memorial Symposium and 5th International Symposium on Nanovision Science: Nanospace Manipulation of Photons and Electrons for Nanovision Systems, in print
23. F. Felder, M. Rahim, M.Fill, H. Zogg N, Quack, S. Blunier, J. Dual, *Lead Salt Resonant Cavity Enhanced Detector with MEMS Mirror*, **Physics Procedia** **3**, 2, Proc. 14th International Conference on Narrow Gap Semiconductors and Systems, pp. 1127-1131, 2010

22. F. Felder, A. Fognini, M. Rahim, M. Fill, E. Müller, H. Zogg, *Formation of Self Assembled PbTe Quantum Dots in CdTe on Si(111)*, **Physics Procedia** **3**, 2, Proc. 14th International Conference on Narrow Gap Semiconductors and Systems, pp. 1121-1125, 2010
21. M. Rahim, A. Khiar, F. Felder, M. Fill, D. Chappuis, H. Zogg, *Above Room Temperature Lead Salt VECSEL*, **Physics Procedia** **3**, 2, Proc. 14th International Conference on Narrow Gap Semiconductors and Systems, pp. 1145-1148, 2010
20. M. Rahim, M. Fill, F. Felder, D. Chappuis, M. Corda, H. Zogg, *Mid-infrared PbTe vertical external cavity surface emitting laser on Si-substrate with above 1 W output power*, **Appl. Phys. Lett.** **95**, 241107, 2009
19. H. Zogg, M. Rahim, A. Khiar, M. Fill, F. Felder, N. Quack, S. Blunier, J. Dual (invited), *IV-VI Mid-IR Tunable Lasers and Detectors with External Resonant Cavities*, **Proc. SPIE** **7453**, 74530R, Infrared Spaceborne Remote Sensing and Instrumentation XVII, 2009
18. H. Zogg, M. Rahim, F. Felder, M. Fill, D. Boye, A. Khiar (invited), *Lead-chalcogenide VECSELs on Si and BaF₂ for 5 μ m emission*, **Proc. SPIE** **7193**, 71931G, Photonics West Solid State Lasers XVIII: Technology and Devices, 2009
17. M. Rahim, A. Khiar, F. Felder, M. Fill, H. Zogg, *4.5 μ m wavelength vertical external cavity surface emitting laser operating above room temperature*, **Appl. Phys. Lett.** **94**, 201112, 2009
16. N. Quack, P. Rüst, S. Blunier, J. Dual, F. Felder, M. Rahim, M. Fill, M. Arnold, H. Zogg, *A Comb Drive Actuated Vertically Moving Micromirror for Mid-Infrared Resonant Cavity Enhanced Detectors*, **Microelectronic Engineering** **86**, pp. 1243-1246, 2009
15. H. Zogg, M. Arnold, F. Felder, M. Rahim, C. Ebnetter, N. Quack, S. Blunier, J. Dual, *Epitaxial lead-chalcogenides on Si for mid-IR detectors and emitters including cavities*, **Proc. AITA** **9**, Advanced Infrared Technology and Applications International Workshop, Leon, Mexico, 2008
14. M. Rahim, F. Felder, M. Fill, H. Zogg, *Optically Pumped 5 μ m IV-VI VECSEL with Al-Heatspreader*, **Optics Letters** **33**, 24, pp. 3010-3012, 2008
13. M. Rahim, F. Felder, M. Fill, D. Boye, H. Zogg, *Lead chalcogenide VECSEL on Si emitting at 5 μ m*, **Electronic Letters** **44**, 25, pp. 1467-1469, 2008

-
12. H. Zogg, M. Arnold, F. Felder, M. Rahim, M. Fill, D. Boye (invited), *Epitaxial lead-chalcogenides on Si for mid-IR detectors and emitters including cavities*, **Proc. SPIE 7082**, 70820H, Infrared Spaceborn Remote Sensing and Instrumentation XVI, 2008
 11. N. Quack, S. Blunier, J. Dual, F. Felder, M. Arnold, H. Zogg, *Mid-Infrared Tunable Resonant Cavity Enhanced Detectors*, **Sensors 2008**, 8 (9), pp. 5466–5478, 2008
 10. H. Zogg, M. Arnold, F. Felder, M. Rahim, C. Ebnetter, I. Zasavitskiy, N. Quack, S. Blunier, J. Dual, *Epitaxial lead-chalcogenides on Si for mid-IR detectors and emitters including cavities*, **Journal of Electronic Materials** **37**, 9, pp. 1497–1503, 2008
 9. N. Quack, S. Blunier, J. Dual, M. Arnold, F. Felder, C. Ebnetter, M. Rahim, H. Zogg, *Vertically Moving Micromirror for Detectors in the Mid Infrared*, **Sensors and Actuators A: Physical**, 143, 1, pp. 29–33, 2008
 8. F. Felder, M. Arnold, C. Ebnetter, M. Rahim, H. Zogg, *Wavelength tunable Resonant Cavity Enhanced Photodetectors based on lead-salts grown by MBE*, **Springer Proceedings in Physics Series 119**, 13th International Conference on Narrow Gap Semiconductors, pp. 143–146, 2008
 7. M. Rahim, M. Arnold, F. Felder, I. Zasavitskiy, H. Zogg, *Mid-Infrared lead-salt VECSEL (Vertical External Cavity Surface Emitting Laser) for Spectroscopy*, **Springer Proceedings in Physics Series 119**, 13th International Conference on Narrow Gap Semiconductors, pp. 143–146, 2008
 6. N. Quack, S. Blunier, J. Dual, M. Arnold, F. Felder, C. Ebnetter, M. Rahim, H. Zogg, *Tunable Resonant Cavity Enhanced Detectors using Vertical MEMS Mirrors*, **Journal of Optics A: Pure and Applied Optics**, 10, 044015, 2008
 5. N. Quack, S. Blunier, J. Dual, M. Arnold, F. Felder, C. Ebnetter, M. Rahim, H. Zogg, *Tunable Resonant Cavity Enhanced Detectors using Vertical MEMS Mirrors*, **Proc. Optical MEMS and Nanophotonics 2007**, Hualien, Taiwan, pp. 165–166, 2007
 4. M. Rahim, M. Arnold, F. Felder, K. Behfar, H. Zogg, *Mid-infrared lead-chalcogenide vertical external cavity surface emitting laser with 5 μm wavelength*, **Appl. Phys. Lett.** **91**, 151102, 2007

3. F. Felder, M. Arnold, M. Rahim, C. Ebnetter, H. Zogg, *Tunable lead-chalcogenide on Si resonant cavity enhanced mid-infrared detector*, **Appl. Phys. Lett.** **91**, 101102, 2007
2. N. Quack, I. Zust, S. Blunier, J. Dual, M. Arnold, F. Felder, M. Rahim, H. Zogg, *Electrostatically actuated Micromirror for Resonant Cavity Enhanced Detectors*, **Proc. MEMS 2007**, 20th IEEE International Conference on MEMS, Kobe, Japan, Jan. 21–25, 2007
1. H. Zogg, M. Arnold, F. Felder, M. Rahim, *Narrow spectral band monolithic lead chalcogenide on Si mid IR photodetectors and high reflectance Bragg mirrors*, **Proc. IWPSD13**, 13th International Workshop on the Physics of Semiconductor Devices, Delhi, India, Dec 13–17, 2005, 7 pages

Conference Presentations

Invited Talks

10. H. Zogg, M. Rahim, M. Fill, F. Felder, A. Khiar, D. Chappuis, *Mid-infrared lead-chalcogenide VECSELs emitting up to above RT at 4–6 μm wavelength*, **LEOS 2009**, 22nd annual Lasers and Electro Optics Society meeting, Belek–Antalya, Turkey, Oct. 4–8, 2009
9. H. Zogg, M. Rahim, A. Khiar, M. Fill, F. Felder, D. Chappuis, N. Quack, S. Blunier, J. Dual, *Mid infrared resonant cavity detectors and lasers with epitaxial lead-chalcogenides*, **EMRS**, Warsaw, Sep. 14–18, 2009
8. H. Zogg, M. Rahim, F. Felder, M. Fill, A. Khiar, D. Chappuis, *Lead chalcogenide mid-IR tunable lasers and narrow band detectors*, **AITA 10**, 10th International Workshop on Advanced Infrared Technology and Applications, Florence, Italy, Sep. 8–11, 2009
7. H. Zogg, M. Rahim, A. Khiar, M. Fill, F. Felder, and N. Quack, *IV–VI Mid-IR Tunable Lasers and Detectors with External Resonant Cavities*, **Infrared Spaceborne Remote Sensing and Instrumentation XVII**, San Diego, CA, USA, Aug. 2–6, 2009

-
6. H. Zogg, M. Rahim, F. Felder, M. Fill, D. Boye, A. Khiar, *Lead-chalcogenide VECSELS on Si and BaF₂ for 5 μ m emission*, **Photonics West Solid State Lasers XVIII: Technology and Devices**, San Jose, CA, USA, Jan. 25–29, 2009
 5. H. Zogg, M. Rahim, F. Felder, M. Fill, D. Boye, *Lead-chalcogenide sensors and lasers for the mid-infrared range*, **10th Takayanagi Kenjiro Memorial Symposium and 5th International Symposium on Nanovision Science: Nanospace Manipulation of Photons and Electrons for Nanovision Systems**, Hamamatsu, Shizuoka University, Japan, Nov. 17–18, 2008
 4. H. Zogg, M. Arnold, F. Felder, M. Rahim, M. Fill, D. Boye, *Epitaxial lead-chalcogenides on Si for mid-IR detectors and emitters including cavities*, **SPIE Infrared Spaceborn Remote Sensing and Instrumentation XVI**, San Diego, CA, USA, Aug. 10–14, 2008
 3. H. Zogg, M. Arnold, F. Felder, M. Rahim, C. Ebnetter, N. Quack, S. Blunier, J. Dual, *Epitaxial lead-chalcogenides on Si for mid-IR detectors and emitters including cavities*, **U.S. Workshop on the physics and chemistry of II–VI materials**, Baltimore, MD, USA, Oct. 30 – Nov. 1, 2007
 2. H. Zogg, M. Arnold, F. Felder, M. Rahim, C. Ebnetter, N. Quack, S. Blunier, J. Dual, *Epitaxial lead-chalcogenides on Si for mid-IR detectors and emitters including cavities*, **AITA 9**, Advanced Infrared Technology and Applications International Workshop, Leon, Mexico, Oct. 8–12, 2007
 1. M. Arnold, F. Felder, M. Rahim, H. Zogg, presented by A. N. Tiwari, *Narrow spectral band monolithic lead-chalcogenide-on-Si mid-IR photodetectors and high reflectance Bragg mirrors*, **IWPSD13**, 13th International Workshop on the Physics of Semiconductor Devices, Delhi, India, Dec. 13–17, 2005

Contributed Talks

25. H. Zogg, M. Rahim, A. Khiar, M. Fill, F. Felder, *4.5 μ m VECSEL (vertical external cavity surface emitting laser) at room temperature*, **SPG 2009**, Innsbruck, Austria, Sep. 2–4, 2009
24. F. Felder, M. Rahim, M. Fill, H. Zogg, N. Quack, S. Blunier, J. Dual, *Lead Salt Resonant Cavity Enhanced Detector with MEMS Mirror*, **NGS-14**, 14th International Conference on

- Narrow Gap Semiconductors and Systems, Sendai, Japan, Jul 13–17, 2009
23. M. Rahim, A. Khair, F. Felder, M. Fill, H. Zogg, *Above Room Temperature Lead Salt VECSEL*, **NGS–14**, 14th International Conference on Narrow Gap Semiconductors and Systems, Sendai, Japan, Jul 13–17, 2009
 22. F. Felder, M. Fill, M. Rahim, N. Quack, S. Blunier, J. Dual, H. Zogg, *Narrow band tunable resonant cavity enhanced detectors for 3 – 10 μm wavelength*, **11th European Symposium on Semiconductor Detectors**, Wildbad Kreuth, Germany, Jun. 7–11, 2009
 21. M. Fill, F. Felder, M. Rahim, H. Zogg, *IV–VI Mid–IR Tunable Lasers and Detectors with External Resonant Cavities*, **39. Freiburg Infrared Colloquium**, Freiburg, Germany, Feb. 17–18, 2009
 20. N. Quack, P. Rüst, S. Blunier, J. Dual, F. Felder, M. Rahim, M. Fill, M. Arnold, H. Zogg, *A Comb Drive Actuated Vertically Moving Micromirror for Mid–Infrared Resonant Cavity Enhanced Detectors*, **MNE 2008**, 34rd International Conference on Micro– and Nano–Engineering, Athens, Greece, Sep. 15–18, 2008
 19. F. Felder, M. Rahim, M. Fill, M. Arnold and H. Zogg, N. Quack, S. Blunier and J. Dual, *Mid–Infrared Tunable Resonant Cavity Enhanced Detectors*, **MIOMD–IX**, 9th International Conference on Mid–Infrared Optoelectronics: Materials and Devices, Freiburg, Germany, Sep. 8–11, 2008
 18. M. Rahim, F. Felder, M. Fill, D. Boye, M. Arnold and H. Zogg, *5 μm Vertical External Cavity Surface Emitting Lasers grown on BaF₂ and Si substrates*, **MIOMD–IX**, 9th International Conference on Mid–Infrared Optoelectronics: Materials and Devices, Freiburg, Germany, Sep. 8–11, 2008
 17. F. Felder, M. Rahim, M. Fill, M. Arnold, H. Zogg, N. Quack, S. Blunier, J. Dual, *Durchstimmbare resonanzverstärkte Detektoren für das mittlere Infrarot*, **DMBE WS08**, Deutscher MBE–Workshop, Zurich, Switzerland, Sep. 1–2, 2008
 16. M. Rahim, F. Felder, M. Fill, M. Arnold and H. Zogg, *5 μm Vertical External Cavity Surface Emitting Lasers grown on BaF₂ and Si substrates*, **DMBE WS08**, Deutscher MBE–Workshop, Zurich, Switzerland, Sep. 1–2, 2008
 15. A. Fognini, F. Felder, M. Rahim, M. Fill and H. Zogg, *Wachstum und Charakterisierung von PbTe Quantendots in CdTe*

Matrix auf Si(111), **DMBE WS08**, Deutscher MBE-Workshop, Zurich, Switzerland, Sep. 1–2, 2008

14. N. Quack, P. Rüst, S. Blunier, J. Dual, M. Arnold, F. Felder, M. Rahim, M. Fill and H. Zogg, *Mid-Infrared Tunable Resonant Cavity Enhanced Detectors Employing Vertically Moving Comb Drive Actuated MEMS Micromirrors*, **Optical MEMS and Nanophotonics 2008**, Freiburg, Germany, Aug 11–14, 2008
13. F. Felder, M. Rahim, M. Fill, M. Arnold, H. Zogg, *Durchstimmbare resonanzverstärkte Detektoren für das mittlere Infrarot*, **38. IR-Kolloquium**, Freiburg, Germany, Mar. 11–12, 2008
12. M. Rahim, F. Felder, M. Fill, M. Arnold, H. Zogg, *Mid-Infrared Vertical External Cavity Surface Emitting Lasers for Spectroscopy*, **38. IR-Kolloquium**, Freiburg, Germany, Mar. 11–12, 2008
11. M. Arnold, M. Rahim, F. Felder, K. Behfar, H. Zogg, *Bleisalz-VECSEL mit 5 μm Emissionswellenlänge*, **DMBE WS07**, Deutscher MBE-Workshop, Hamburg, Germany, Oct. 1–2, 2007
10. F. Felder, M. Arnold, M. Rahim, H. Zogg, *Durchstimmbare resonanzverstärkte Photodetektoren für das mittlere Infrarot*, **DMBE WS07**, Deutscher MBE-Workshop, Hamburg, Germany, Oct. 1–2, 2007
9. N. Quack, S. Blunier, J. Dual, M. Arnold, F. Felder, C. Ebnetter, M. Rahim, H. Zogg, *Tunable Resonant Cavity Enhanced Detectors using Vertical MEMS Mirrors*, **Optical MEMS and Nanophotonics 2007**, Hualien, Taiwan, Aug. 12–16, 2007
8. M. Rahim, M. Arnold, F. Felder, I. Zasavitskiy, H. Zogg, *Mid-Infrared Vertical External Cavity Surface Emitting Lasers for Spectroscopy*, **NGS-13**, 13th International Conference on narrow Gap Semiconductors, Guilford, UK, Jul. 8–12, 2007
7. M. Arnold, F. Felder, C. Ebnetter, M. Rahim, N. Quack, S. Blunier, J. Dual, H. Zogg, *Wavelength tunable resonant cavity enhanced detectors*, **MIOMD-VIII**, 8th International Conference on Mid-Infrared Optoelectronics: Materials and Devices, Bad Ischl, Austria, May 14–16, 2007
6. M. Rahim, M. Arnold, F. Felder, H. Zogg, *Mid-Infrared Vertical External Cavity Surface Emitting Lasers grown by MBE*, **37. IR-Kolloquium**, Freiburg, Germany, Mar 27–28, 2007
5. F. Felder, M. Arnold, M. Rahim, C. Ebnetter, H. Zogg, *Resonant Cavity Photodetektoren mit durchstimmbarer Wellenlänge*

- im mittleren Infrarot*, **37. IR-Kolloquium**, Freiburg, Germany, Mar 27–28, 2007
4. M. Arnold, F. Felder, M. Rahim, N. Quack, S. Blunier, H. Zogg, *Resonant Cavity Photodetektoren für Infrarotsensoren mit durchstimmbarer Wellenlänge*, **DMBE WS06**, Deutscher MBE-Workshop, Hamburg, Germany, Sep. 26–27, 2006
 3. M. Rahim, M. Arnold, F. Felder, H. Zogg, I. Zasavitskiy, *Vertical External Cavity Surface Emitting Laser (VECSEL) for the Mid-Infrared with IV–VI Compounds*, **DMBE WS06**, Deutscher MBE-Workshop, Hamburg, Germany, Sep. 26–27, 2006
 2. F. Felder, M. Rahim, M. Arnold, H. Zogg, *Komponenten für VECSEL im mittleren Infrarot*, **36. IR-Kolloquium**, Freiburg, Germany, April 4–5, 2006
 1. M. Rahim, M. Arnold, F. Felder, H. Zogg, *High Reflectivity curved Bragg mirrors for the mid-infrared*, **DMBE WS05**, Deutscher MBE-Workshop, Stuttgart, Germany, October 11–12, 2005

Poster Presentations

15. N. Quack, S. Blunier, J. Dual, F. Felder, M. Fill, M. Rahim, H. Zogg, *Micro Gas Analyzer for the mid-Infrared, CTI Micro and Nano Technologies: The Impact of Miniaturization*, Neuchatel, Switzerland, Nov. 11, 2009
14. A. Fognini, F. Felder, M. Rahim, M. Fill, H. Zogg, *Formation of Self Assembled PbTe Quantum Dots in CdTe on Si(111)*, **NGS-14**, 14th International Conference on Narrow Gap Semiconductors and Systems, Sendai, Japan, Jul 13–17, 2009
13. M. Rahim, A. Khlar, F. Felder, M. Fill, D. Chappuis, M.W. Sigrist, H. Zogg, *5 μm Vertical External Cavity Surface Emitting Lasers (VECSEL) for Spectroscopic Applications*, **TDLS 2009**, 7th International Conference on Tunable Diode Laser Spectroscopy, Zermatt, Switzerland, Jul. 13–17, 2009
12. N. Quack, S. Blunier, J. Dual, M. Arnold, F. Felder, M. Rahim, H. Zogg, *Electrostatically Actuated Micromirrors for Resonant Cavity Enhanced Detectors*, **MicroNanoFabrication Annual Review Meeting**, Lausanne, Switzerland, May 19, 2009
11. A. Fognini, F. Felder, M. Rahim, M. Fill and H. Zogg, *Self assembled PbTe quantum dots in CdTe on Si(111)*, **MIOMD-**

-
- IX**, 9th International Conference on Mid-Infrared Optoelectronics: Materials and Devices, Freiburg, Germany, Sep. 8–11, 2008
10. N. Quack, P. Rust, S. Blunier, J. Dual, M. Arnold, F. Felder, M. Rahim, H. Zogg, *Electrostatically Actuated Micromirrors for Resonant Cavity Enhanced Detectors*, **MicroNanoFabrication Annual Review Meeting**, Lausanne, Switzerland, May 20, 2008
 9. N. Quack, S. Blunier, J. Dual, M. Arnold, F. Felder, M. Rahim, H. Zogg, **Micro and Nanosystems Platform Industry Day**, Zurich, Switzerland, Mar. 19, 2008
 8. N. Quack, S. Blunier, J. Dual, M. Arnold, F. Felder, C. Ebnetter, M. Rahim, H. Zogg, *MEMS Mirrors for the use in Resonant Cavity Enhanced Detectors*, **MNE 2007**, 33rd International Conference on Micro- and Nano-Engineering, Copenhagen, Denmark, Sep. 23–26, 2007
 7. F. Felder, M. Arnold, C. Ebnetter, M. Rahim, H. Zogg, N. Quack, S. Blunier, J. Dual, *Wavelength tunable Resonant Cavity Enhanced Photodetectors based on lead-salts grown by MBE*, **NGS-13**, 13th International Conference on narrow Gap Semiconductors, Guilford, UK, Jul. 8–12, 2007
* Student Presentation Prize (best poster)
 6. M. Rahim, M. Arnold, F. Felder, I. Zasavitskiy, H. Zogg, *Mid-Infrared vertical external cavity surface emitting lasers grown by MBE*, **MIOMD-VIII**, 8th International Conference on Mid-Infrared Optoelectronics: Materials and Device, Bad Ischl, Austria, May 14–16, 2007
 5. N. Quack, S. Blunier, J. Dual, M. Arnold, F. Felder, M. Rahim, H. Zogg, *Electrostatically Actuated Micromirrors for Resonant Cavity Enhanced Detectors*, **MicroNanoFabrication Annual Review Meeting**, Lausanne, Switzerland, May 8, 2007
 4. M. Rahim, M. Arnold, F. Felder, I. Zasavitsky, H. Zogg, *Mid-Infrared Vertical External Cavity Surface Emitting Lasers grown by MBE*, **EUROMBE 14**, 14th European Molecular Beam Epitaxy Workshop, Granada, Spain, Mar. 5–7, 2007
 3. F. Felder, M. Arnold, M. Rahim, C. Ebnetter, H. Zogg, N. Quack, S. Blunier, J. Dual, *Narrowband Resonant Cavity Enhanced mid-IR Photodetectors tuneable within a broad wavelength region*, **EUROMBE 14**, 14th European Molecular Beam Epitaxy Workshop, Granada, Spain, Mar. 5–7, 2007

2. N. Quack, S. Blunier, J. Dual, M. Arnold, F. Felder, M. Rahim, H. Zogg, *Electrostatically actuated Micromirror for Resonant Cavity Enhanced Detectors*, **MEMS 2007**, 20th IEEE International Conference on MEMS, Kobe, Japan, Jan. 21–25, 2007
1. M. Arnold, D. Zimin, F. Felder, H. Zogg, *Resonant Cavity Enhanced Photodetectors for the Mid-Infrared Range*, **EUROMBE 13**, 13th European Molecular Beam Epitaxy Workshop, Grindelwald, Switzerland, March 7–9, 2005

Acknowledgements

This thesis, could not have be done without the help and involvement of a lot of people. They all have my sincere thanks:

- Hans Zogg, for the opportunity to write this thesis, for the productive cooperation and his continuous support, and for everything else,
- Danilo Pescia and Jürg Dual, for beeing coexaminers,
- Niels Quack and Stefan Blunier from the Center of Mechanics, for the rewarding collaboration,
- the IV-VI PhDs Martin Arnold, Mohamed Rahim and Matthias Fill, it was always nice working with you,
- the diploma students Christian Ebeneter, for doing the piezo dance, and Andreas Fognini, for the dashes,
- Elisabeth Müller and Peter Wägli from the EMEZ, for the STEM and SEM images,
- the TFP craftspeople, Oliver Meier and Jachen Däscher, for fixing anything broken,
- the PV PhDs and such, including the guys from Flisom, and the guests, for being around,
- Juliane, per se.

So Long, and Thanks for All the Fish.